

1 Computational determination of a primary diffusion mode in
2 γ U-10Mo under irradiation

3 Gyuchul Park^a, Benjamin Beeler^{b,c}, Maria A. Okuniewski^{a,*}

4 ^a*School of Materials Engineering, Purdue University, West Lafayette, IN 47907, United States*

5 ^b*Department of Nuclear Engineering, North Carolina State University, Raleigh, NC 27695, United States*

6 ^c*Idaho National Laboratory, Idaho Falls, ID 83415, United States*

7 **Abstract**

Low enriched uranium (< 20 % ^{235}U)-molybdenum (U-Mo) monolithic fuel is the primary candidate for high-performance research and test reactors and is in the process of being qualified to replace highly-enriched uranium ($\geq 20\%$ ^{235}U) fuel. As part of the qualification process, it is critical to understand and predict the behavior of fission gas bubbles under irradiation, which affects fuel swelling and fuel failure. Mechanistic fuel models are being developed that can both reproduce the existing experimental data for fuel swelling, and be further applied to irradiation conditions beyond the experimental scope. Diffusion of species under irradiation conditions is an important parameter in the mechanistic fuel models; however, no temperature-relevant experimental diffusion data exists. In the present work, radiation-enhanced diffusion coefficients of U, Mo, and Xe in γ U-10wt.%Mo were calculated in the temperature range between 300 K and 1400 K via rate-theory models and molecular dynamics simulations with an embedded-atom method interatomic potential for the U-Mo-Xe system. Accordingly, total diffusion coefficients under relevant irradiation conditions are determined using previously obtained intrinsic thermal diffusion and radiation-driven diffusion coefficients, as well as the newly calculated radiation-enhanced diffusion coefficients presented herein. Radiation-enhanced diffusion of U and Mo was dominant in the intermediate temperature range, whereas radiation-enhanced diffusion of Xe did not significantly contribute to total diffusion of Xe at the relevant fission rate densities. Radiation-enhanced diffusion of Xe became faster than both intrinsic thermal diffusion and radiation-driven diffusion at a fission rate density of 5×10^{22} fissions/m³/s, which is higher than the typical fission rate density range in research reactors. The temperature regime where radiation-enhanced diffusion of each element dominated was dependent on the fission rate density. The total diffusion coefficients of U, Mo, and Xe, updated in this work, will be utilized as parameters in the mechanistic fuel models to help predict the behavior of fission gas bubbles under irradiation more accurately.

8 **Keywords:** uranium-molybdenum (U-Mo) alloys, Xe, fission gas, intrinsic thermal

9 diffusion, radiation-enhanced diffusion, rate-theory model, molecular dynamics

10 **1. Introduction**

11 There are currently five high-performance research reactors (HPRR) and one critical as-
12 semby fueled by highly-enriched uranium (HEU, $\geq 20\% \text{ }^{235}\text{U}$) in the United States (US):
13 the Advanced Test Reactor and Advanced Test Reactor Critical Assembly at Idaho National
14 Laboratory, the High Flux Isotope Reactor at Oak Ridge National Laboratory, the Mas-
15 sachusetts Institute of Technology Reactor, the National Bureau of Standards Reactor, and
16 the University of Missouri Research Reactor. Under the USHPRR program, initiated and
17 developed by the US Department of Energy and the Office of Material Management and
18 Minimization in the National Nuclear Security Administration, there have been substantial
19 efforts to convert HEU-based fuels to low enriched uranium (LEU, $< 20\% \text{ }^{235}\text{U}$) based fuels
20 to limit nuclear proliferation risks. LEU-molybdenum monolithic fuel was selected as a nu-
21 clear fuel material and design due to its high uranium density (17.3 g U/cm^3 for LEU-7Mo
22 monolithic fuel), dimensional stability, mechanical integrity, and stable swelling behavior at
23 high fission densities (up to $7.2 \times 10^{27} \text{ fissions/m}^3$) [1, 2, 3, 4, 5, 6]. LEU-10Mo monolithic
24 fuel is currently in the process of being experimentally tested and qualified to be utilized as
25 fuel for HPRRs [7, 8, 9].

26 Microstructural evolution of nuclear fuel under irradiation is a complicated process, in-
27 fluenced by a number of unique phenomena, ranging from the atomic scale to the microscale,
28 which affects the macroscopic properties of fuel. During reactor operation, an atom located
29 in a lattice can be removed from its lattice site if it undergoes a collision with an energetic
30 particle and receives sufficient kinetic energy. Primary knock-on atoms (PKAs) can create
31 secondary knock-on atoms which displace tertiary knock-on atoms, etc., ultimately resulting
32 in the creation of various types of defects such as interstitials, vacancies, dislocation loops,
33 and voids. This phenomenon, referred to as a displacement cascade, is the initiation point of
34 irradiation damage with a length-scale of nm and a time-scale of ps [10]. Noble gases such as
35 Xe and Kr, referred to as gaseous fission products, are also produced from the fission of ^{235}U
36 nuclei and have low solubility in the fuel matrix. The insoluble gaseous fission products tend
37 to coalesce and form fission gas bubbles through a diffusion process both inside the grains
38 (intragranular fission gas bubbles) and along the grain boundaries (intergranular fission gas
39 bubbles). In U-10Mo fuels, it was found that the intragranular fission gas bubbles were
40 considerably smaller than the intergranular fission gas bubbles [1, 11, 12]. The size of the
41 intergranular fission gas bubbles was a few hundreds of nm at a fission density of $2-3 \times 10^{27}$
42 fiss/m³ [1, 11], while the size of the intragranular fission gas bubbles was approximately 1-2
43 nm in diameter, and formed in a superlattice at a fission density of $1.41 \times 10^{27} \text{ fiss/m}^3$

[12]. Larger intragranular fission gas bubbles (3.5 nm in diameter) were observed at a higher fission density of 4.5×10^{27} fiss/m³ [13], indicating that the size of the intragranular fission gas bubbles grows slowly with increasing fission density. However, the intragranular fission gas bubbles tend not to grow above a certain size due to re-solution [14]. The fission gas bubbles are destroyed and re-solved through the interaction with energetic fission fragments, and the re-solved fission gas atoms occupy the U-Mo body-centered cubic (bcc) lattice [14]. As fission density increases further, U-Mo fuel goes through grain refinement, historically referred to as recrystallization, and provides additional nucleation sites for intergranular fission gas bubbles, thereby accelerating fuel swelling [15, 16, 17].

Modeling and simulation play a pivotal role in understanding and predicting the microstructural evolution of fuel under irradiation conditions to facilitate fuel qualification. For instance, the behavior of fission gas bubbles in U-Mo fuel under irradiation has been studied primarily with phase-field models [18, 19, 20, 21]. In addition, U-Mo fuel swelling mechanistic models, as implemented in the Dispersion Analysis Research Tool (DART) code, are currently being developed to incorporate experimental observations and measurements, thus enabling the prediction of U-Mo fuel swelling beyond the current experimental burn-up regime [22, 23]. Diffusion coefficients of the species in U-Mo under irradiation conditions are critical parameters in the mechanistic fuel model; however, experimental data does not exist at the relevant research reactor temperatures or under irradiation. This lack of knowledge has motivated the current study of diffusion of the species (U, Mo, and Xe) in γ U-10Mo under irradiation conditions.

Turnbull et al. [24] reported that diffusion of fission gas in UO₂ under irradiation is dominated by three different diffusion components depending on the temperature: intrinsic thermal diffusion in the high-temperature regime (> 1600 K), radiation-enhanced diffusion in the intermediate temperature regime (between 1200 K and 1600 K), and radiation-driven diffusion in the low-temperature regime (< 1200 K), at a fission rate density of 10^{19} fiss/m³/s. The intrinsic thermal diffusion is driven by the defect concentration at equilibrium. Intrinsic thermal diffusion of Xe in UO₂ [25], calculated via DFT calculations, agreed well with the experimental observations [24]. Similar studies of U, Si, and Xe component-based diffusion have also been explored in U₃Si₂ accident tolerant fuel [26, 27]. To the best of the authors' knowledge, no Xe intrinsic thermal diffusion data in U-Mo fuel exists. For the purposes of lower length scale modeling, it has been initially assumed that the intrinsic thermal diffusion of Xe is slower than the intrinsic diffusion of U by approximately four orders of magnitude in γ U-Mo [19, 28, 29]. Intrinsic thermal diffusion of U and Mo in γ U-10Mo at research reactor temperatures can be extrapolated from high-temperature experiments (from 923 K to 1273K) by fitting the experimental data [30] into the determined Arrhenius equation. Thus,

80 the accepted equations of intrinsic thermal diffusion (D_{INT} in m^2/s) for U, Mo, and Xe in
 81 γ U-10Mo are as follows [19, 28, 29, 30]:

$$D_{INT}^U = 1.28 \times 10^{-5} \times \exp(-1.76/kT), \quad (1)$$

$$D_{INT}^{Mo} = 1.62 \times 10^{-5} \times \exp(-1.97/kT), \quad (2)$$

$$D_{INT}^{Xe^1} = 1.28 \times 10^{-9} \times \exp(-1.76/kT), \quad (3)$$

82 where k is the Boltzmann constant and T is the temperature in Kelvin (K).

83 Radiation-driven diffusion, controlled by ballistic mixing due to collision cascades, was
 84 previously found to be athermal and dependent on the fission fragment kinetic energy from
 85 a single fission event and the associated species' mean-squared displacements, which are
 86 dependent on the PKA energy density [27]. It should be noted that defects can be also
 87 produced via not only collision cascades, but also the transfer of energy deposited by fission
 88 fragments into the electronic subsystem (thermal spike) [31, 32]. It was assumed that the
 89 effects of the thermal spike were negligible. Radiation-driven diffusion (D_{RDD} in m^2/s) of
 90 U, Mo, and Xe in γ U-10Mo, calculated by Beeler et al. [27], is described as follows:

$$D_{RDD}^U = 1.97 \times 10^{-41} \times \dot{F}, \quad (4)$$

$$D_{RDD}^{Mo} = 2.01 \times 10^{-41} \times \dot{F}, \quad (5)$$

$$D_{RDD}^{Xe} = 5.07 \times 10^{-41} \times \dot{F}, \quad (6)$$

91 where \dot{F} is the fission rate density in fiss/ m^3/s .

92 Radiation-enhanced diffusion is governed by enhanced defect concentrations under irra-
 93 diation. Radiation-enhanced diffusion in UO_2 and U_3Si_2 was investigated through cluster
 94 dynamics calculations parametrized by DFT calculations and MD simulations [25, 33, 34].
 95 Radiation-enhanced diffusion coefficients of species in γ U-Mo do not exist, which has moti-
 96 vated the current study.

97 In this work, the radiation-enhanced diffusion (D_{RED}) of U, Mo, and Xe is determined
 98 utilizing a rate-theory model parametrized using MD simulations. Intrinsic thermal diffusion
 99 of Xe in γ U-10Mo is additionally determined using MD simulations with the assumption that
 100 Xe diffusion is facilitated by a vacancy. The total diffusion coefficients (D_{TOT}) of U, Mo, and

¹⁰¹ Xe in γ U-Mo under irradiation conditions are also presented as a summation of the three
¹⁰² diffusion components, given in Eqn. 7, in the temperature range between 300 K and 1400 K
¹⁰³ and in the fission rate density range between 5×10^{18} fiss/m³/s and 5×10^{22} fiss/m³/s.

$$D_{TOT} = D_{INT} + D_{RED} + D_{RDD}. \quad (7)$$

¹⁰⁴ **2. Computational Details**

¹⁰⁵ *2.1. Interatomic Potential*

¹⁰⁶ Molecular dynamics is a simulation method capable of generating the trajectory of atoms
¹⁰⁷ (or molecules) in a given system. The force acting on each atom can be calculated by numer-
¹⁰⁸ ically integrating Newton's equations of motion with the initial positions and velocities of
¹⁰⁹ atoms in the system. The reliability of MD simulations is highly dependent on the accuracy
¹¹⁰ of the interatomic potential utilized. In this work, an embedded-atom method (EAM) inter-
¹¹¹ atomic potential was used to perform MD simulations with the LAMMPS software package
¹¹² [35]. The accuracy of the EAM formalism comes from its description of many-body interac-
¹¹³ tions, which does not exist within pairwise potentials.

¹¹⁴ A general form of the EAM interatomic potential, developed by Daw and Baskes, is
¹¹⁵ described as follows [36, 37]:

$$E_T = \sum_{i < j} \phi_{ij}(r_{ij}) + \sum_i F\left(\sum_{j \neq i} \rho_i(r_{ij})\right), \quad (8)$$

¹¹⁶ where E_T is the total energy of the system, ϕ_{ij} is the pair potential function, which is
¹¹⁷ dependent on the distance (r_{ij}) between the two given atoms i and j . The term F is the
¹¹⁸ embedding energy of atom i , which depends on the spatially-dependent electron density
¹¹⁹ and determines the many-body interatomic interactions. Each atom is regarded as being
¹²⁰ embedded in the background electron density, and the electron density is dependent on
¹²¹ the neighboring atoms. In this work, the EAM potential for the ternary U-Mo-Xe system,
¹²² developed by Smirnova et al. [38], was used. This potential was fitted to the first principles
¹²³ data including forces and energies using the force-matching method [39]. The U-Mo-Xe
¹²⁴ ternary EAM interatomic potential was chosen in this work since the material properties,
¹²⁵ including the lattice parameter, thermal expansion coefficient, Young's modulus, and melting
¹²⁶ temperature of U-10Mo alloys were in agreement with the experimental observations [38].
¹²⁷ Additionally, this is the only interatomic potential currently available that describes the
¹²⁸ ternary U-Mo-Xe system.

¹²⁹ 2.2. Atomistic modeling of the diffusion of U, Mo, and Xe

¹³⁰ A supercell of 10 x 10 x 10 unit cells (2,000 atoms) of γ U was created with periodic
¹³¹ boundary conditions. Such a relatively large supercell was utilized to produce the random
¹³² substitutional solid solution alloys and to avoid the interaction of the Xe-vacancy clusters
¹³³ across periodic boundary conditions. Twenty-three percent of the U atoms were replaced
¹³⁴ with Mo atoms, corresponding to a 10 wt.% bcc random solid substitutional alloy. The sys-
¹³⁵ tem was relaxed for 200 ps with a timestep of 0.002 ps in an NPT ensemble with a Langevin
¹³⁶ thermostat in the Gronbech-Jenson-Farago formalism [40, 41]. This has been previously
¹³⁷ identified to be more than sufficient for the appropriate relaxation of such a system [42].
¹³⁸ Subsequently, a defect (vacancy/self-interstitial/Xe-vacancy cluster) was separately created
¹³⁹ in the system, and the system was relaxed for another 200 ps. Xe diffusion in U-Mo was
¹⁴⁰ based on the assumption that Xe diffuses via vacancy clustering, as observed in other fuel
¹⁴¹ materials [25, 43, 44, 45, 46]. Interstitial diffusion is not considered in the calculations of the
¹⁴² radiation-enhanced diffusion of Xe. The formation energy of a Xe interstitial atom is greater
¹⁴³ than the summation of the formation energy of substitutional Xe atom and self-interstitial
¹⁴⁴ atom (U or Mo) in γ U-10Mo [47, 48, 49]. Additionally, the energetics of Xe defects dictated
¹⁴⁵ that Xe interstitials will generate a self-interstitial and reside as a substitutional atom, pro-
¹⁴⁶ viding justification for neglecting an interstitial mechanism [47, 48, 49]. Due to the extremely
¹⁴⁷ slow diffusion of Xe, the diffusion coefficient of Xe in a vacancy cluster was calculated with
¹⁴⁸ respect to the vacancy cluster size. The schematics of the Xe-vacancy cluster arrangements
¹⁴⁹ in γ U-10Mo considered in this work are represented in Fig. 1. The atomic positions of both
¹⁵⁰ U and Mo atoms surrounding a Xe atom, randomly distributed in a substitutional manner
¹⁵¹ in a bcc lattice, were considered vacant sites. Vacancy and interstitial diffusion coefficients
¹⁵² of U and Mo ($D_{v/i}^{U/Mo}$), and the diffusion coefficient of Xe in a vacancy cluster (D_{nvac}^{Xe}) were
¹⁵³ calculated with the slope of the mean-squared displacement with time as follows:

¹⁵⁴

$$D_{v/i/nvac}^{U/Mo/Xe} = \frac{\sum_{i=1}^N \langle \Delta r_i^2 \rangle}{6t}, \quad (9)$$

¹⁵⁵

¹⁵⁶ where $\langle \Delta r_i^2 \rangle$ is the mean-squared displacement of the i^{th} atom and t is the simulation time.
¹⁵⁷ The mean-squared displacements of U and Mo in the system were obtained for 100 ns. Since
¹⁵⁸ the diffusion of Xe was extremely slow when compared to U and Mo in the temperature
¹⁵⁹ regime investigated, a longer time period of 500 ns was required. Twenty simulations were
¹⁶⁰ conducted from 800 K to 1400 K for U and Mo, and from 1000 K to 1400 K for Xe. The
¹⁶¹ obtained diffusion coefficients were averaged.

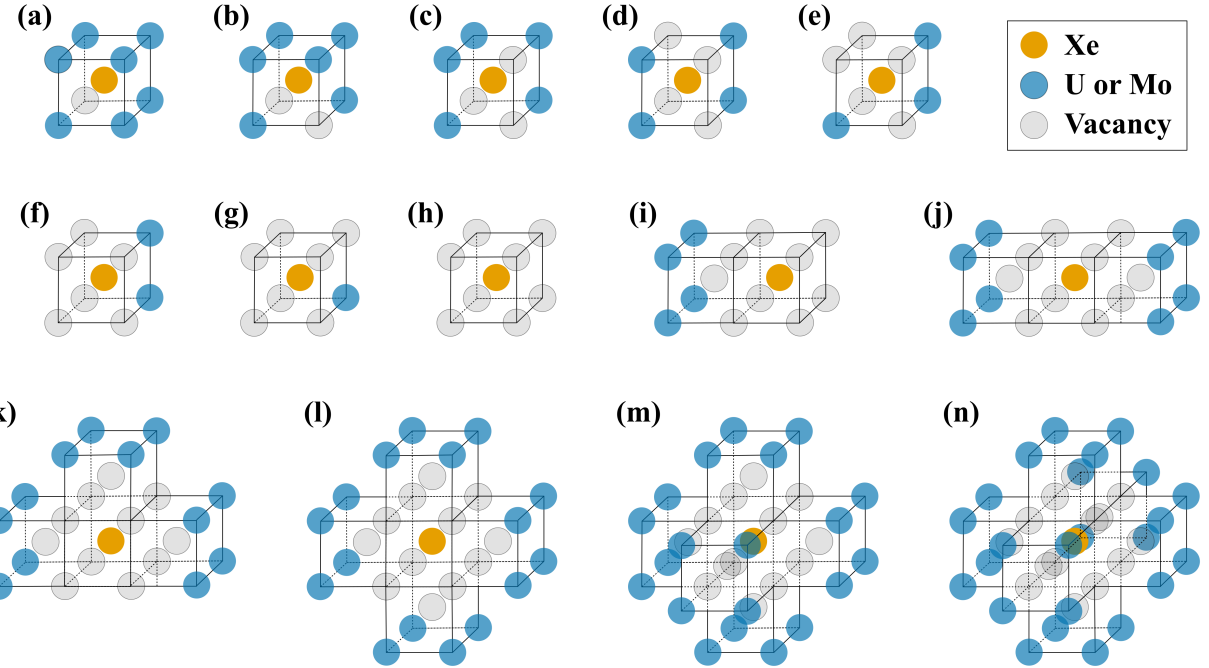


Figure 1: Schematics of the Xe-vacancy clusters in γ U-10Mo considered in the present work: (a) Xe-monovacancy ($n=1$), (b) Xe-divacancy ($n=2$), (c) Xe-trivacancy ($n=3$), (d) Xe-quadvacancy ($n=4$), (e) Xe-pentavacancy ($n=5$), (f) Xe-hexavacancy ($n=6$), (g) Xe-heptavacancy ($n=7$), (h) Xe-octavacancy ($n=8$), (i) Xe-nonavacancy ($n=9$), (j) Xe-decavacancy ($n=10$), (k) Xe-undecavacancy ($n=11$), (l) Xe-dodecavacancy ($n=12$), (m) Xe-tridecavacancy ($n=13$), and (n) Xe-tetradecavacancy ($n=14$), where n is the number of vacancies in a Xe cluster. Blue spheres represent the matrix U-Mo, yellow spheres represent Xe, and grey spheres represent vacant sites.

162

163 *2.3. Steady-State Defect Concentration under Irradiation*

164 The steady-state concentration of vacancies and interstitials under irradiation conditions
165 can be obtained by solving the coupled differential equations as follows:

$$\frac{dC_v}{dt} = \epsilon \dot{F} - K_{iv} C_i C_v - k_{vs}^2 D_v C_v, \quad (10)$$

$$\frac{dC_i}{dt} = \epsilon \dot{F} - K_{iv} C_i C_v - k_{is}^2 D_i C_i, \quad (11)$$

166 where C_v is the concentration of vacancies, C_i is the concentration of interstitials, ϵ is the
167 defect production rate per fission event, K_{iv} is the recombination rate constant between va-
168 cancies and interstitials, k_{vs}^2 is the sink strength of grain boundaries for vacancies, k_{is}^2 is the
169 sink strength of grain boundaries for interstitial atoms, D_v is the vacancy diffusion coeffi-
170 cient, and D_i is the interstitial diffusion coefficient. Sinks were restricted to grain boundaries

¹⁷¹ in this work (e.g., dislocation sinks were neglected). The coupled differential equations were
¹⁷² solved using the Rosenbrock solver (Rodas-4) with Julia [50, 51].

¹⁷³ The defect production rate (ϵ) was calculated from the athermal recombination corrected
¹⁷⁴ dpa (arc-dpa) model [52], which is a modification of the NRT dpa model [53] which calcu-
¹⁷⁵ lates the number of atomic displacements. The arc-dpa model takes into account thermally
¹⁷⁶ activated recombination, resulting in a decrease in the number of defects existing under ir-
¹⁷⁷ radiation as compared to the NRT dpa model [52]. The number of defects generated (N_d) is
¹⁷⁸ described by the arc-dpa model as:

¹⁷⁹

$$N_d = \frac{0.8T_d}{2E_d}\xi, \quad (12)$$

¹⁸⁰

¹⁸¹ where T_d is the damage energy, E_d is the threshold displacement energy, and ξ is the arc-dpa
¹⁸² efficiency function [52]. The damage energy is taken as the kinetic energy of the fission frag-
¹⁸³ ments produced from a fission reaction (approximately 170 MeV), and reduced to account for
¹⁸⁴ electronic energy losses. It is assumed that only ballistic effects generate Frenkel pairs. The
¹⁸⁵ electronic energy losses have been previously calculated to be 95%, thus the damage energy
¹⁸⁶ used is 8.5 MeV [27]. The magnitude of the threshold displacement energy for γ U-10Mo
¹⁸⁷ is not well known, but can potentially be determined from MD simulations or from experi-
¹⁸⁸ ments. Given that such studies are beyond the scope of this work, reasonable approximations
¹⁸⁹ are made for the threshold displacement energy (60 eV) based upon MD simulations in γ U
¹⁹⁰ [54], and for the arc-dpa efficiency (0.25), which is approximately the same as bcc Fe [52].
¹⁹¹ This yields approximately 14,000 point defects per fission event in γ U-10Mo. The defect
¹⁹² production rate was obtained by dividing the number of generated defects per fission event
¹⁹³ by the atomic number density of γ U-10Mo. Any bias towards interstitial atoms or vacancies
¹⁹⁴ in the defect production process is neglected, assuming that an equal number of both types
¹⁹⁵ of defects are generated. The number of point defects generated in a fission event for this
¹⁹⁶ work utilized calculations from Beeler et al. [27], which generally agreed with the estimates
¹⁹⁷ from Kolotova et al. [32].

¹⁹⁸ In order to determine the recombination rate constant (K_{iv}), separate MD simulations
¹⁹⁹ were conducted. A supercell of 40 x 40 x 40 unit cells (128,000 atoms) of γ U was generated
²⁰⁰ with an atomic composition of 10 wt.% of Mo with periodic boundary conditions. Fifty
²⁰¹ Frenkel pairs were created, ensuring that the distance between individual defects is at least
²⁰² $4a_0$, where a_0 is the lattice constant. The system was equilibrated for 20,000 timesteps with
²⁰³ a variable timestep such that a maximum distance for an atom to move in one timestep is
²⁰⁴ 5 fm, in order to perform a constrained relaxation of the defects. Subsequently, the system

205 was evolved for 10 ns with a timestep of 1 fs, tracking the number of Frenkel pairs as a
206 function of time via the Voronoi occupation methodology within the LAMMPS. This com-
207 putational setup is in line with previous efforts to determine recombination rate constants
208 utilizing MD [55]. This defect evolution simulation was performed from 600 K to 1200 K
209 in increments of 100 K. For a given temperature, the number of defects (C_0) as a function
210 of time can be fit to $C = C_0/(C_0 K_{iv} t + 1)$, where C_0 is the initial concentration of Frenkel
211 pairs. In classical rate theory, the grain boundaries are constant sinks and their strength,
212 k^2 , is estimated as $15/L^2$ (L is the grain size, in units of nm) for grain boundaries with a
213 regular pattern, and is identical for both interstitials and vacancies. This assumption is uti-
214 lized here as a first approximation, and along with a grain size estimate of 10 μm , completes
215 the parameterization of the rate theory equations. The grain size is defined as the aver-
216 age diameter of the grains. It should be noted that the steady-state concentration of defects
217 increased with increasing grain size, and saturated when the grain size was greater than 1 μm .

218

219 *2.4. Xe-Vacancy Cluster Concentration under Irradiation*

220 A separate rate-theory formulation was constructed with the assumption that Xe, the
221 most common fission product [56], was continuously produced in the system, and thus Xe-
222 vacancy clusters with various sizes were also present. Xe-vacancy clusters containing up to
223 fourteen vacancies were taken into account, as mentioned previously. For instance, the first
224 and second nearest neighbor shells are completely composed of vacancies near a Xe atom
225 within a bcc lattice in a Xe-tetravacancy cluster ($n=14$). The rate of change in defect con-
226 centrations including Xe and Xe-vacancy clusters with time can be mathematically described
227 as follows:

$$\frac{dC_v}{dt} = \epsilon \dot{F} - K_{iv} C_i C_v - k_{vs}^2 D_v C_v \quad (13)$$

$$+ \sum_{n=1}^{14} \alpha_{n+1} C_{Xe-nv} - \sum_{n=1}^{13} \beta_n C_v C_{Xe-(n-1)v} + \sum_{n=1}^{13} n R C_{Xe-nv},$$

$$\frac{dC_i}{dt} = \epsilon \dot{F} - K_{iv} C_i C_v - k_{is}^2 D_i C_i, \quad (14)$$

$$\frac{dC_{Xe}}{dt} = \tau \dot{F} - \beta_1 C_v C_{Xe} + \alpha_2 C_{Xe-1v} + \sum_{n=1}^{14} R C_{Xe-nv}, \quad (15)$$

$$\frac{dC_{Xe-1v}}{dt} = \beta_1 C_v C_{Xe} - \beta_2 C_v C_{Xe-1v} - \alpha_2 C_{Xe-1v} + \alpha_3 C_{Xe-2v} - R C_{Xe-1v}, \quad (16)$$

$$\frac{dC_{Xe-2v}}{dt} = \beta_2 C_v C_{Xe-1v} - \beta_3 C_v C_{Xe-2v} - \alpha_3 C_{Xe-2v} + \alpha_4 C_{Xe-3v} - R C_{Xe-2v}, \quad (17)$$

$$\frac{dC_{Xe-3v}}{dt} = \beta_3 C_v C_{Xe-2v} - \beta_4 C_v C_{Xe-3v} - \alpha_4 C_{Xe-3v} + \alpha_5 C_{Xe-4v} - R C_{Xe-3v}, \quad (18)$$

⋮

$$\frac{dC_{Xe-14v}}{dt} = \beta_{14} C_v C_{Xe-13v} - \alpha_{15} C_{Xe-14v} - R C_{Xe-14v}, \quad (19)$$

228 where C_{Xe} is the Xe concentration, C_{Xe-nv} is the concentration of a Xe cluster containing
 229 n vacancies, τ is the yield of Xe from fission reactions where $\tau = 0.13$ [57], β_n is the absorption
 230 coefficient, α_n is the emission coefficient, and R is the re-solution rate of a Xe-vacancy
 231 cluster where $R = 2.0 \times 10^{-24} \times \dot{F}$ (s^{-1}) [58]. The absorption and emission coefficients were
 232 calculated by Eqns. 20 and 21 [59]:

233

$$\beta_n = \frac{4\pi(r_0 + r_n)D_v}{V_{at}}, \quad (20)$$

$$\alpha_{n+1} = \beta_n \exp\left(\frac{-E_n^b}{kT}\right), \quad (21)$$

234

235 where r_0 is the radius of a single vacancy, r_n is the radius of a Xe-vacancy cluster containing
 236 n vacancies, and E_n^b is the binding energy of the n^{th} vacancy in a Xe cluster containing n
 237 vacancies. Assuming all clusters are spherical, $r_n = (\frac{3nV_{at}}{4\pi})^{1/3}$, where V_{at} is the volume per
 238 atom for the bcc crystal structure, given by $V_{at} = \frac{a_0^3}{2}$. The binding energy of the n^{th} vacancy
 239 in a Xe cluster containing n vacancies (E_n^b) was calculated as in Eqn. 22:

240

$$E_n^b = E_{Xe-(n+1)vac}^f - E_{Xe-nvac}^f - E_v^f, \quad (22)$$

241

242 where $E_{Xe-nvac}^f$ is the formation energy of a Xe cluster containing n vacancies, $E_{Xe-(n+1)vac}^f$
 243 is the formation energy of a Xe cluster containing $n+1$ vacancies, and E_v^f is the vacancy
 244 formation energy. The vacancy formation energy in γ U-10Mo was assumed to be 1.6 eV
 245 [49].

246 Separate MD simulations were also performed to calculate the formation energies of a
 247 Xe-vacancy cluster in γ U-10Mo. A supercell of 10 x 10 x 10 unit cells of γ U was created
 248 with periodic boundary conditions. Twenty-three percent of the U atoms in the system were
 249 substituted by Mo atoms to produce γ U-10Mo. The system was equilibrated for 200 ps at
 250 the evaluated temperatures (from 400 K to 1400 K in increments of 200 K) in an NPT en-
 251 semble with a Langevin thermostat in the Gronbech-Jenson-Farago formalism [40, 41] with
 252 a timestep of 0.002 ps. Subsequently, various sizes of the Xe-vacancy clusters were created in
 253 the system separately (Fig. 1), and the system was equilibrated for another 200 ps. The for-
 254 mation energies of a Xe cluster containing n and $n+1$ vacancies ($E_{Xe-nvac}^f$ and $E_{Xe-(n+1)vac}^f$)
 255 were calculated as in Eqns. 23 and 24:

256

$$E_{Xe-nvac}^f = E_{Xe-nvac} - \frac{\{N - (n + 1)\}}{N} E_{ideal}, \quad (23)$$

$$E_{Xe-(n+1)vac}^f = E_{Xe-(n+1)vac} - \frac{\{N - (n + 2)\}}{N} E_{ideal}, \quad (24)$$

257

258 where E_{ideal} is the potential energy of the system containing no defects, $E_{Xe-nvac}$ is the po-
 259 tential energy of the system containing a Xe cluster with n vacancies, $E_{Xe-(n+1)vac}$ is the
 260 potential energy of the system containing a Xe cluster with $n+1$ vacancies, and N is the
 261 number of atoms in the system. Numerous simulations were conducted until the cumulative
 262 moving average of the potential energy of each system converged to consider different con-
 263 figurational environments (U and Mo) in the alloy [42]. Thus, two hundred simulations were
 264 performed, and the potential energies were averaged at each temperature.

265

266 2.5. Radiation-enhanced Diffusion of U, Mo, and Xe in γ U-10Mo

267 Given a steady-state concentration of vacancies and interstitials under irradiation and the
 268 diffusion coefficients of vacancies and interstitials, the radiation-enhanced diffusion coefficient

²⁶⁹ (D_{RED}) of U and Mo can be expressed as follows [60]:

$$D_{RED}^U = D_v^U C_v^{irr} + D_i^U C_i^{irr}, \quad (25)$$

$$D_{RED}^{Mo} = D_v^{Mo} C_v^{irr} + D_i^{Mo} C_i^{irr}, \quad (26)$$

²⁷⁰

²⁷¹ where D_v^U is the vacancy diffusion coefficient of U, D_v^{Mo} is the vacancy diffusion coefficient of
²⁷² Mo, D_i^U is the interstitial diffusion coefficient of U, D_i^{Mo} is the interstitial diffusion coefficient
²⁷³ of Mo, C_v^{irr} is the steady-state concentration of vacancies under irradiation, and C_i^{irr} is the
²⁷⁴ steady-state concentration of interstitials under irradiation. Unlike U and Mo, it is assumed
²⁷⁵ that the diffusion of Xe occurs through vacancy clustering, and thus the radiation-enhanced
²⁷⁶ diffusion coefficient of Xe can be described as follows [60]:

²⁷⁷

$$D_{RED}^{Xe} = \sum_{n=1}^{k-1} D_{nvac}^{Xe} C_{Xe-nvac}^{irr}, \quad (27)$$

²⁷⁸

²⁷⁹ where and $C_{Xe-nvac}^{irr}$ is the concentration of a Xe cluster containing n vacancies under irradiation.
²⁸⁰ It was assumed that Xe-vacancy clusters do not interact with each other. As will be
²⁸¹ discussed, in order to approximate losses to large bubbles, the largest Xe-vacancy clusters
²⁸² are considered immobile.

²⁸³ 2.6. Intrinsic Thermal Diffusion of Xe in γ U-10Mo

²⁸⁴ The intrinsic thermal diffusion coefficient of Xe in γ U-10Mo was also calculated since
²⁸⁵ both experimental and computational data do not exist. In addition, the previously utilized
²⁸⁶ value of the intrinsic thermal diffusion coefficient of Xe is based on the hypothesis that the
²⁸⁷ intrinsic thermal diffusion of Xe is slower than that of U by four orders of magnitude [19].
²⁸⁸ With the assumption that diffusion of Xe is mediated by a vacancy [25, 43, 44, 45, 46], the
²⁸⁹ intrinsic thermal diffusion of Xe ($D_{INT}^{Xe^2}$) can be calculated under the same computational
²⁹⁰ parameters described in Section 2.2 as follows:

²⁹¹

$$D_{INT}^{Xe^2} = c_v D_{1vac}^{Xe}, \quad (28)$$

²⁹²

²⁹³ where c_v is the vacancy concentration at equilibrium and D_{1vac}^{Xe} is the diffusion coefficient of
²⁹⁴ Xe in a mono-vacancy cluster. The concentration of vacancies at equilibrium was calculated
²⁹⁵ using the equation as follows:

$$c_v = \exp\left(\frac{\Delta S_v^f}{k_B}\right) \exp\left(\frac{-E_v^f}{k_B T}\right), \quad (29)$$

where ΔS_v^f is the change in entropy introduced from creating a vacancy. The equilibrium vacancy concentration is not affected by the entropy term, as has been previously assumed in diffusional studies in γ U-Mo [42, 61].

3. Results

3.1. Recombination Rate Constant

The number of defects was determined as a function of time in the temperature range between 600 K and 1200 K in increments of 100 K. Fig. 2(a) represents the defect concentration with respect to time in γ U-10Mo at 1000 K, as an example. Temperatures below 600 K were not explored, as intrinsic diffusion on MD timescales is very limited below 600 K in γ U-10Mo. It can be observed that the number of defects decays as a function of time in a near-exponential fashion, with the rate of annihilation slowing as a function of time due to the decreased number of defects present. The fit to the data is also shown in Fig. 2(a), which provides a value of the recombination rate constant (K_{iv}) at 1000 K. For each individual temperature analyzed, the recombination rate constant is calculated from the defect concentration as a function of time. Fig. 2(b) represents the recombination rate constant from 600 K to 1200 K along with the power function fit.

According to kinetic theory [60], the recombination rate constant can be estimated as $K_{iv} = 4\pi(D_v + D_i)r_{iv}/V_{at}$, where r_{iv} is the interstitial-vacancy recombination radius. Typical values of the recombination radius are on the order of 2-3 times the equilibrium lattice constant (a_0) [62, 63]. By utilizing the fit values of the recombination rate constant and the known diffusion coefficients and equilibrium volume, the recombination radius can be determined. It is found that the recombination radius is significantly larger than what is typically observed. For example, at 1000 K, the recombination radius is approximately $8a_0$. As the temperature decreases, the recombination radius increases farther, such that the distance of the recombination radius at 600 K is $24a_0$. Considerably larger recombination radii ($3.5-15a_0$) were also observed in UO_2 , which is in agreement with the present work [64]. It is assumed that this is due to the long stress field interactions between interstitials and vacancies, leading to rapid recombination. This perhaps compensates for the low interstitial formation energies in γ U systems, such that the large number of defects that are created can also rapidly recombine. Such a phenomenon was hinted at in previous studies of displacement energies in γ U [54].

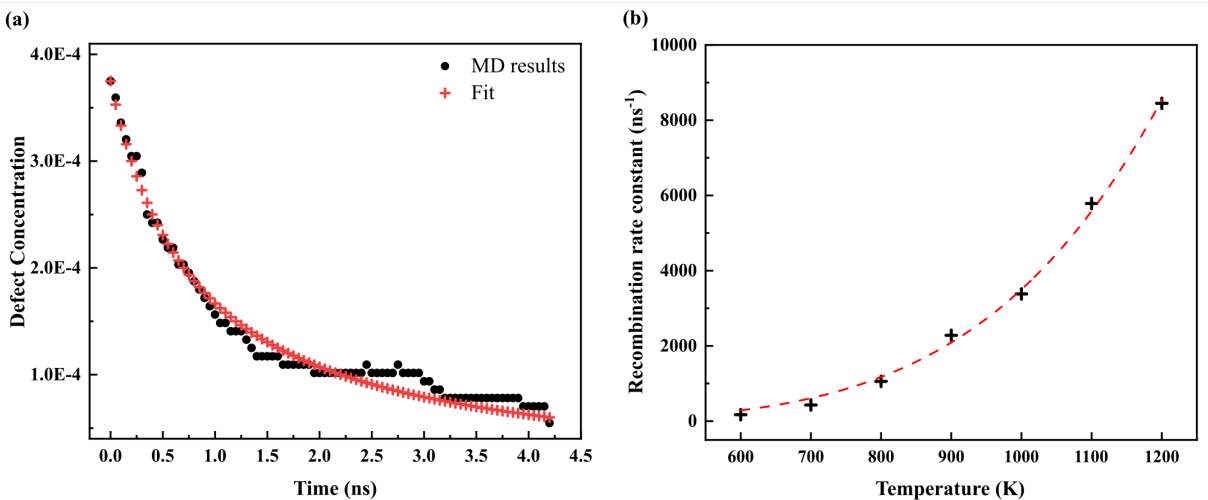


Figure 2: (a) The evolution of Frenkel pair concentration as a function of time at 1000 K, accounting for recombination. (b) Recombination rate constants (K_{iv}) as a function of temperature.

326 3.2. Radiation-enhanced Diffusion of U and Mo

327 Implementing the recombination rate constant from Section 3.1, Eqns. 10 and 11 are
 328 used to determine the steady-state concentration of point defects under irradiation as a
 329 function of temperature in γ U-10Mo at three different fission rate densities. Fig. 3(a) shows
 330 the evolution of the concentration of vacancies and interstitials at the fission rate density of
 331 5×10^{20} fiss/m³/s at 1000 K, as an example. It took approximately 0.2 s for the concentra-
 332 tion of both vacancies and interstitials to reach steady-state under these conditions. With
 333 decreasing temperature, it takes longer for the concentrations of vacancies and interstitials
 334 to reach the steady-state, as expected. The steady-state concentrations of vacancies and
 335 interstitials as a function of temperature are shown at three different fission rate densities
 336 in Fig. 3(b). As the temperature increases, the number of vacancies and interstitials recom-
 337 bining increases, resulting in a decrease in the steady-state concentration of vacancies and
 338 interstitials. The concentration of vacancies was higher than the concentration of intersti-
 339 tials since the interstitials, which diffuse faster than vacancies, diffused into sinks such as
 340 grain boundaries [42, 65]. The concentration of vacancies decreased more rapidly than the
 341 concentration of interstitials with increasing temperature. This implies that the diffusion of
 342 vacancies is more sensitive to temperature than the diffusion of interstitials.

343 Fig. 4(a) shows the vacancy and interstitial diffusion coefficients of U and Mo in γ U-10Mo
 344 as a function of temperature. The calculated diffusion coefficients were extrapolated to lower
 345 temperatures by fitting to an Arrhenius equation. The calculation of vacancy and interstitial
 346 diffusion of U and Mo (D_v^U , D_i^U , D_v^{Mo} , and D_i^{Mo}) in γ U-10Mo was previously conducted by
 347 the authors [42], and additional MD calculations were conducted at 900 K, 1100 K, 1300
 348 K, and 1400 K to improve statistics within this work. The diffusion via interstitial atoms

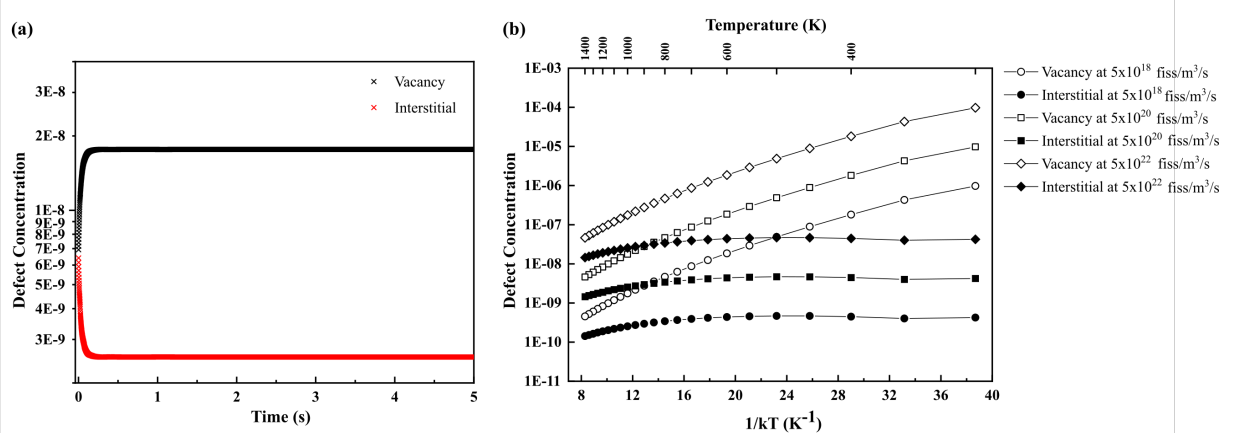


Figure 3: (a) Evolution of concentration of vacancies and interstitials as a function of time at the fission rate density of 5×10^{20} fiss/m³/s at 1000 K, as an example. (b) Rate theory calculations of the defect concentration evolution as a function of inverse temperature at three fission rate densities (units are fiss/m³/s). Note that the y-axis is shown in a log scale.

349 was faster than diffusion via vacancies in the evaluated temperature range, indicating that
 350 the diffusion in γ U-10Mo takes place primarily via interstitial atoms [42, 65]. Vacancy and
 351 interstitial diffusion of U and Mo ($D_v^{U/Mo}$ and $D_i^{U/Mo}$) were insignificant below 900 K and
 352 800 K, respectively, within the MD timescales. The results of the Arrhenius fits for vacancy
 353 and interstitial diffusion of U and Mo are given in Table 1.

354 Using the steady-state concentration of vacancies and interstitials, as well as the diffusion
 355 coefficients of vacancies and interstitials, the radiation-enhanced diffusion coefficients of U
 356 and Mo in γ U-10Mo were calculated, as shown in Fig. 4(b), as a function of temperature
 357 at three fission rate densities. The radiation-enhanced diffusion of U was found to be faster
 358 than that of Mo, originating from the higher interstitial diffusion coefficient of U. The effect
 359 of the fission rate density on radiation-enhanced diffusion of U and Mo was evaluated, and
 360 a square root dependence of the radiation-enhanced diffusion coefficient was observed, as
 361 expected [26, 34]. A coefficient for fission-rate dependence can be obtained by dividing the
 362 total radiation-enhanced diffusion by the square root of the fission rate density. Thus, the
 363 total diffusion coefficients of U and Mo in γ U-10Mo, respectively, under irradiation can be
 364 obtained by the summation of intrinsic thermal diffusion, radiation-enhanced diffusion, and
 365 radiation-driven diffusion as follows:

366

$$D_U = 1.28 \times 10^{-5} \times \exp\left(-\frac{1.76}{kT}\right) + 1.10 \times 10^{-26} \times \exp\left(-\frac{0.38}{kT}\right) \times \sqrt{\dot{F}} + 1.97 \times 10^{-41} \times \dot{F}, \quad (30)$$

$$D_{Mo} = 1.62 \times 10^{-5} \times \exp\left(-\frac{1.97}{kT}\right) + 2.10 \times 10^{-27} \times \exp\left(-\frac{0.39}{kT}\right) \times \sqrt{\dot{F}} + 2.01 \times 10^{-41} \times \dot{F}. \quad (31)$$

367

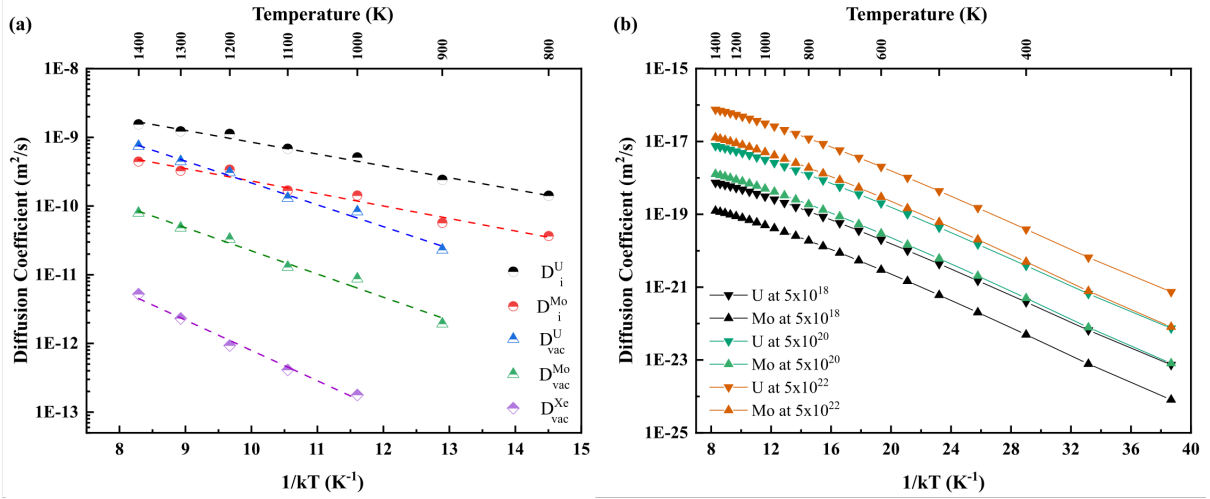


Figure 4: (a) Vacancy and interstitial diffusion coefficients of U, Mo, and Xe. (b) Radiation-enhanced diffusion of U and Mo at three fission rate densities (units are fiss/m³/s).

368

Table 1: Arrhenius fits of vacancy and interstitial diffusion of U, Mo, and Xe in γ U-10Mo.

Parameter	Migration energy (eV)	Pre-exponential factor (m ² /s)
D_i^U	0.40	4.49×10^{-8}
D_i^{Mo}	0.42	1.52×10^{-8}
D_v^U	0.73	3.28×10^{-7}
D_v^{Mo}	0.78	5.27×10^{-8}
D_v^{Xe}	1.02	2.06×10^{-8}

369 Radiation-enhanced diffusion of U and Mo in γ U-10Mo is displayed alongside intrinsic
 370 diffusion and radiation-driven diffusion as a function of inverse temperature at three fission
 371 rate densities in Fig. 5 (a)-(c) and Fig. 6 (a)-(c), respectively. Intrinsic diffusion of U
 372 and Mo, calculated via both experiments and MD simulations, are included for comparison
 373 purposes [30, 42]. The intrinsic diffusion calculated using MD simulations [42], is signifi-
 374 cantly higher than the experimental intrinsic diffusion [30]. The disparity in the intrinsic

375 diffusion, determined via experiments [30] and MD simulations [42], likely originates from
376 the microstructural features. The intrinsic diffusion, calculated via MD simulations, is not
377 affected by the microstructure since the simulations represented an ideal alloy system with-
378 out defect sinks. Conversely, the experimental results can be influenced by sink features
379 such as dislocations, grain boundaries, and impurities in the alloys, resulting in a decrease in
380 intrinsic diffusion. In addition, in the calculation of intrinsic diffusion using MD simulations
381 [42], there were only three intrinsic diffusion data points for U and Mo above 800 K since
382 diffusion of U and Mo below 800 K was insignificant within the MD timescale. Thus, the ex-
383 trapolation using three data points at high temperatures may not be a good assumption for
384 lower temperatures. Therefore, the experimental intrinsic diffusion is utilized for comparison
385 to determine the primary diffusion mechanism during research reactor operating conditions.

386

387 When compared to the experimental intrinsic diffusion [30], the radiation-enhanced diffu-
388 sion of U and Mo dominated in the intermediate temperature range, depending on the fission
389 rate density. With increasing fission rate densities, the minimum temperature at which
390 radiation-enhanced diffusion dominated increased, and the range of temperatures where
391 radiation-enhanced diffusion is prevalent decreased. Specifically, the radiation-enhanced dif-
392 fusion of U becomes the primary mode of diffusion between 350 K and 600 K at 5×10^{18}
393 fiss/m³/s (Fig. 5(a)), 450 K and 650 K at 5×10^{20} fiss/m³/s (Fig. 5(b)), and 550 K and
394 700 K at 5×10^{22} fiss/m³/s (Fig. 5(c)). The radiation-enhanced diffusion of Mo dominated
395 in the temperature ranges between 450 K and 650 K at 5×10^{18} fiss/m³/s (Fig. 6(a)) and
396 550 K and 700 K at 5×10^{20} fiss/m³/s (Fig. 6(b)). Above the temperature ranges specified,
397 intrinsic thermal diffusion was dominant, while below this temperature range radiation-
398 driven diffusion was dominant. The intrinsic thermal diffusion of Mo became faster than
399 the radiation-enhanced diffusion and the radiation-driven diffusion of Mo above 750 K, and
400 the radiation-driven diffusion of Mo became faster than the intrinsic thermal diffusion and
401 the radiation-enhanced diffusion of Mo below 750 K at 5×10^{22} fiss/m³/s (Fig. 6(c)). This
402 decreasing prevalence of radiation-enhanced diffusion with increasing fission rate density is
403 due to the square-root dependency on the fission rate density, while radiation-driven diffu-
404 sion exhibits a linear dependency on the fission rate density. Thus, the rate of increase of
405 the radiation-driven diffusion with increasing fission rate density surpasses that of radiation-
406 enhanced diffusion. The total diffusion coefficients of U and Mo (including all three diffusion
407 modes) are represented as a function of inverse temperature at three fission rate densities in
408 Fig. 5 (d) and Fig. 6 (d), respectively.

409

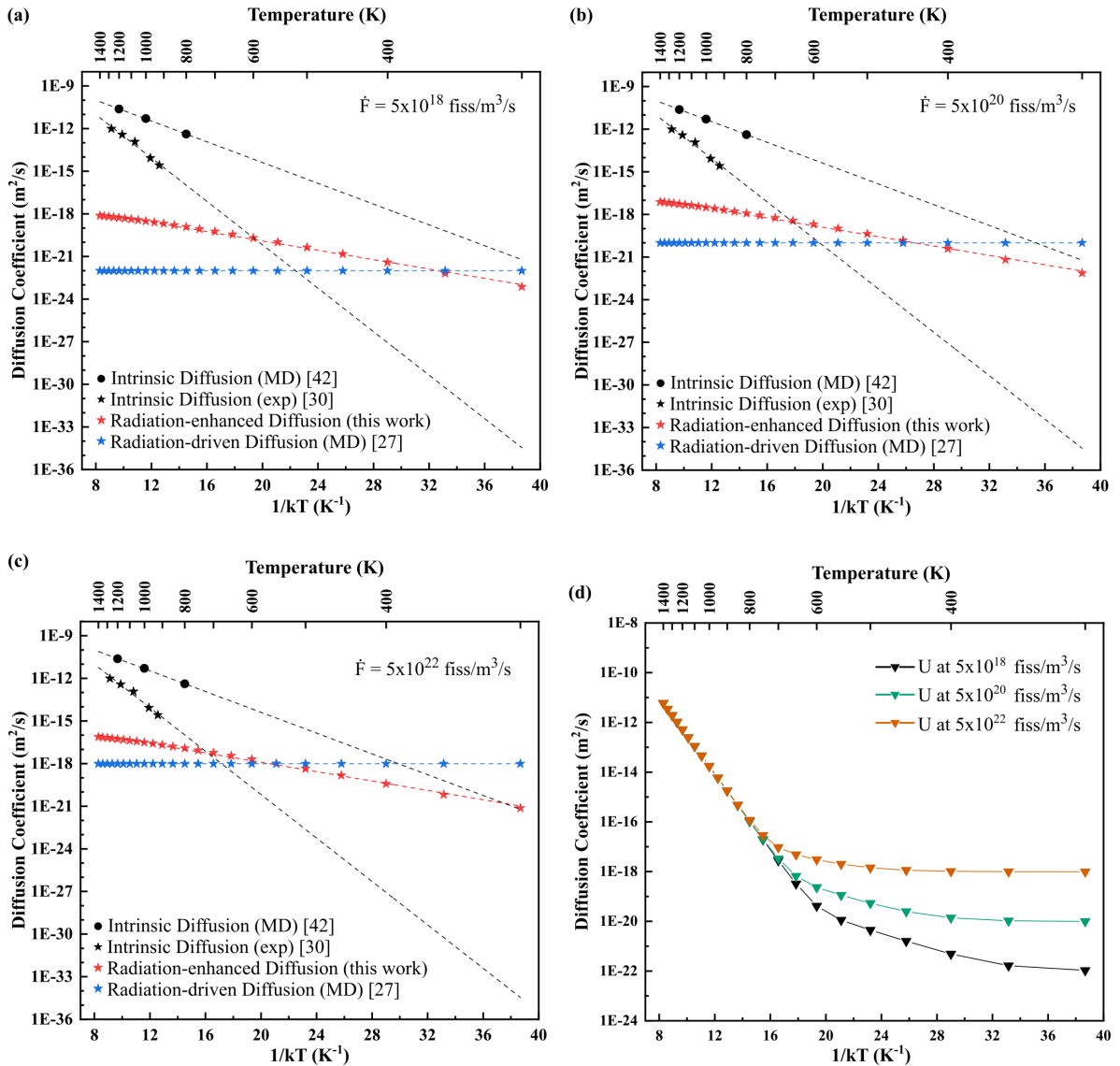


Figure 5: Intrinsic diffusion, radiation-enhanced diffusion, and radiation-driven diffusion of U in γ -U-10Mo (a) at $5 \times 10^{18} \text{ fiss}/m^3/s$, (b) at $5 \times 10^{20} \text{ fiss}/m^3/s$, and (c) at $5 \times 10^{22} \text{ fiss}/m^3/s$. (d) Total diffusion of U in γ -U-10Mo at three fission rate densities in $\text{fiss}/m^3/s$.

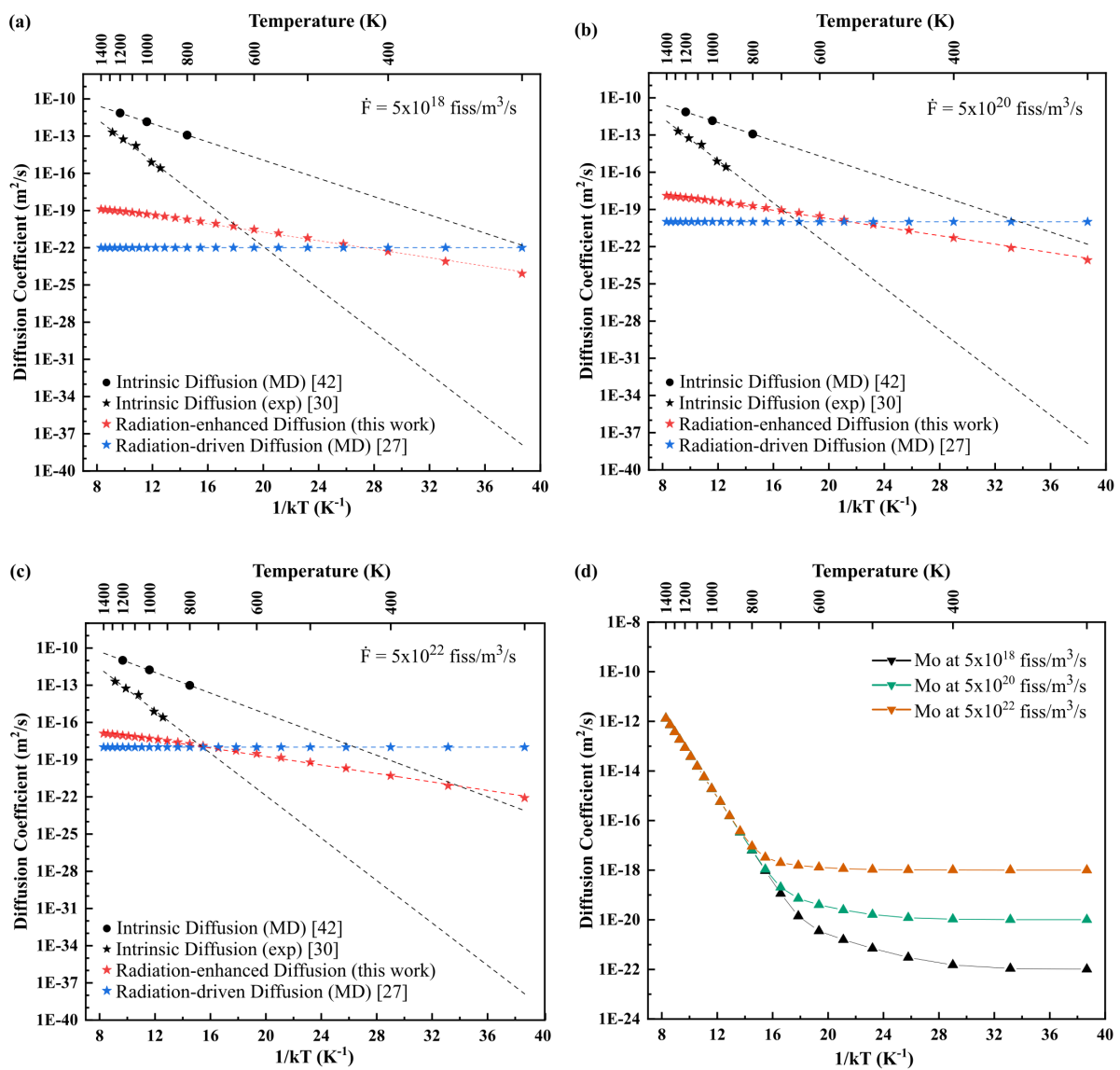


Figure 6: Intrinsic diffusion, radiation-enhanced diffusion, and radiation-driven diffusion of Mo in γ -U-10Mo (a) at $5 \times 10^{18} \text{ fiss}/m^3/s$, (b) at $5 \times 10^{20} \text{ fiss}/m^3/s$, and (c) at $5 \times 10^{22} \text{ fiss}/m^3/s$. (d) Total diffusion of Mo in γ -U-10Mo at three fission rate densities in $\text{fiss}/m^3/s$.

410 3.3. Radiation-enhanced Diffusion of Xe

411 The formation energies of substitutional Xe and Xe-vacancy clusters are calculated as
 412 a function of cluster size and temperature as shown in Fig. 7(a). The formation energies
 413 of the substitutional Xe and the Xe-vacancy clusters increased approximately in a linear
 414 fashion with increasing temperature. The formation energy of each Xe-vacancy cluster was
 415 fitted linearly, and the binding energies were estimated from the fit value of the formation
 416 energies. The estimated binding energy of the n^{th} vacancy in a Xe cluster with n vacancies is
 417 represented with respect to the Xe cluster size at 1000 K in Fig. 7(b), where $n = 1, 2, 3$, and
 418 4, as an example. The binding energies of the n^{th} vacancy in a Xe cluster with n vacancies
 419 became higher (more negative) with increasing Xe-vacancy cluster sizes. The binding energy
 420 of a Xe cluster containing more than four vacancies was estimated using a linear fit at each
 421 temperature from 300 K to 1400 K in increments of 50 K.

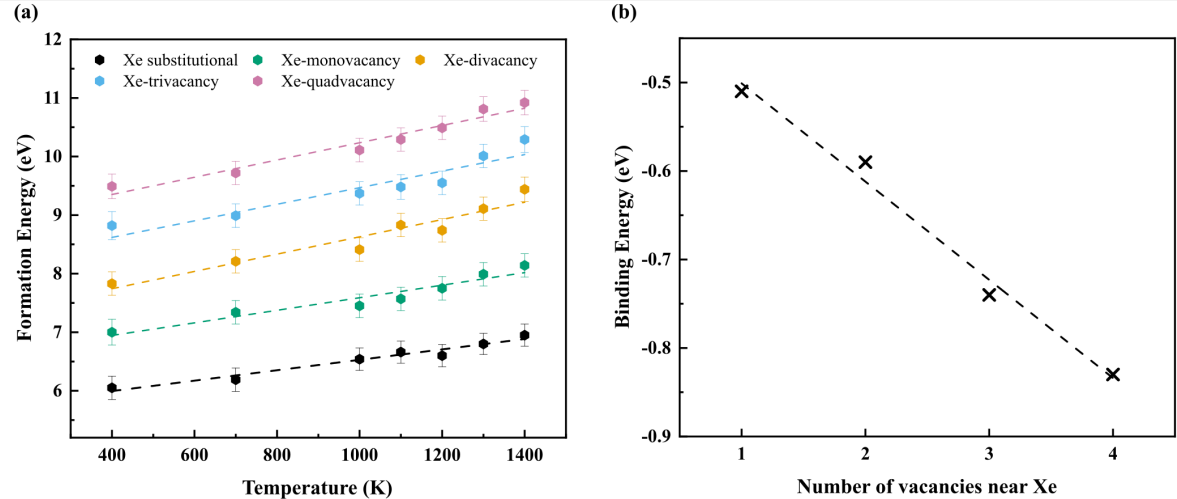


Figure 7: (a) Formation energies of Xe-vacancy clusters as a function of temperature. (b) Binding energies of n^{th} vacancy in a Xe cluster containing n vacancies at 1000 K, where $n = 1, 2, 3$, and 4 as an example.

422 Given the formation energies and binding energies of all Xe-vacancy clusters of interest,
 423 the absorption and emission coefficients in Eqns. 20 and 21 can be determined and the
 424 rate-theory formulation outlined in Eqns. 13-19 can be implemented. The steady-state con-
 425 centrations of defects, including vacancies, interstitials, Xe substitutionals, and Xe-vacancy
 426 clusters, are calculated as a function of inverse temperature at three fission rate densities in
 427 Fig. 8. The temperature interval was 50 K in the range above 700 K, and the interval was
 428 decreased to 25 K below 700 K to show the smooth transition in the defect concentrations.
 429 The concentration of the Xe clusters including vacancies up to only four (quadvacancy) are
 430 represented for the sake of simplicity in Fig. 8. Complete data of the defect concentrations
 431 with respect to inverse temperature at three different fission rate densities is included in the

⁴³² Appendix.

⁴³³ The steady-state concentrations of Xe-vacancy clusters were dependent on the temper-
⁴³⁴ ature, exhibiting three distinct regimes. In the low-temperature regime, the smallest Xe-
⁴³⁵ vacancy cluster (the Xe-monovacancy cluster) had the highest concentration, followed by
⁴³⁶ the Xe-divacancy cluster, the Xe-trivacancy cluster, and the Xe-quadvacancy cluster. This
⁴³⁷ corresponds to temperatures less or equal to 300 K at 5×10^{18} fiss/m³/s, 325 K at 5×10^{20}
⁴³⁸ fiss/m³/s, and 400 K at 5×10^{22} fiss/m³/s. In the low-temperature regime, there are a suffi-
⁴³⁹ cient number of vacancies present to allow for clustering due to the low recombination rate
⁴⁴⁰ constant (Fig. 2(b)). However, a small Xe-vacancy cluster is not able to absorb a large
⁴⁴¹ number of vacancies and grow into a bigger vacancy cluster since the diffusion of vacancies
⁴⁴² is extremely slow. In the intermediate temperature range, there are still a sufficient number
⁴⁴³ of vacancies present, and the diffusion of vacancies is sufficiently high to allow for absorp-
⁴⁴⁴ tion of vacancies by an existing Xe-vacancy cluster, resulting in the highest concentration of
⁴⁴⁵ the biggest Xe-vacancy cluster. This intermediate regime corresponds to the temperatures
⁴⁴⁶ between 325 K and 500 K at 5×10^{18} fiss/m³/s, 400 K and 575 K at 5×10^{20} fiss/m³/s, and
⁴⁴⁷ 450 K and 625 K at 5×10^{22} fiss/m³/s. In the high-temperature regime, the concentration of
⁴⁴⁸ all of the existing Xe-vacancy clusters started to decrease as the temperature increased. The
⁴⁴⁹ population of vacancies was dramatically reduced at high temperatures due to the high re-
⁴⁵⁰ combination rate constant and the high diffusivity leading to Frenkel pair annihilation. Thus,
⁴⁵¹ there are not enough residual vacancies to interact with the Xe species. As the temperature
⁴⁵² increased, the concentration of larger Xe-vacancy clusters decreased more rapidly than the
⁴⁵³ concentration of smaller Xe-vacancy clusters. As a result, the concentration of the biggest
⁴⁵⁴ Xe-vacancy cluster had the lowest concentration, while the concentration of the smallest
⁴⁵⁵ Xe-vacancy cluster, Xe-monovacancy cluster, had the highest concentration. The high tem-
⁴⁵⁶ perature regime corresponds to temperatures greater than 575 K at 5×10^{18} fiss/m³/s, 625 K
⁴⁵⁷ at 5×10^{20} fiss/m³/s, and 700 K at 5×10^{22} fiss/m³/s. Thus, these three temperature regimes
⁴⁵⁸ are delineated by changes in the mobility of vacancies and the temperature dependence of
⁴⁵⁹ the recombination rate. It should be emphasized that these trends are applicable for all Xe
⁴⁶⁰ cluster sizes investigated (up to the Xe-tetradecavacancy cluster), as displayed in Fig. A.1
⁴⁶¹ for clarity.

⁴⁶²

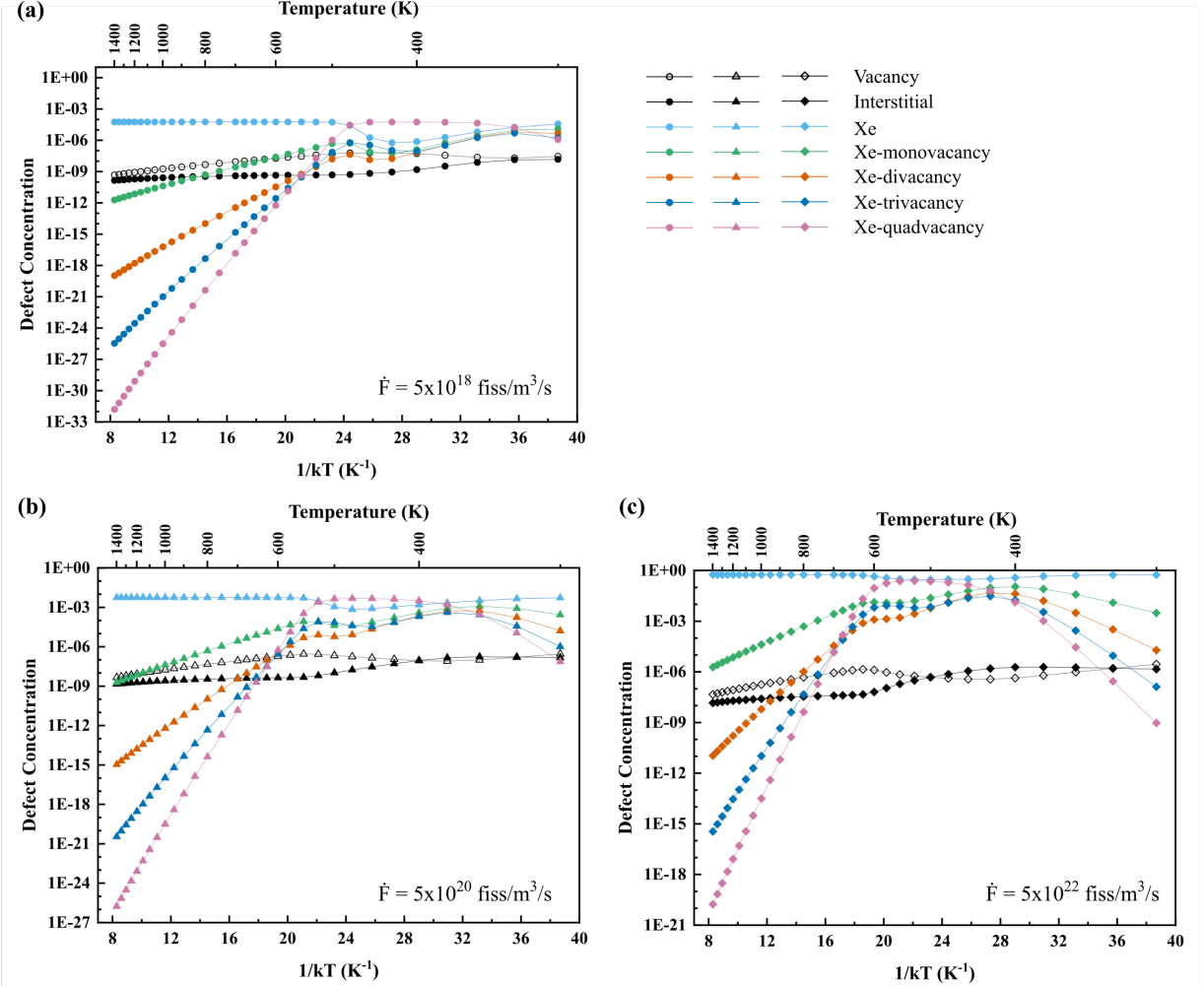


Figure 8: Evolution of defect concentrations in γ U-10Mo as a function of inverse temperature at (a) 5×10^{18} fiss/m³/s, (b) 5×10^{20} fiss/m³/s, and (c) 5×10^{22} fiss/m³/s. Note the differences in the y scales.

In order to utilize the Xe-cluster concentrations for Xe radiation-enhanced diffusion calculations in γ U-10Mo, the individual diffusion coefficients of each cluster must be known, as outlined in Eqn. 9. The diffusion coefficients of Xe in a vacancy cluster with respect to cluster size and temperature as calculated via MD simulations are represented in Fig. 9(a). The diffusion coefficients of Xe in a vacancy cluster were negligible below 1000 K within the MD timescales. It was expected that the diffusion coefficient of Xe would decrease with increasing vacancy cluster size. However, interestingly, the diffusion coefficients of Xe clusters were effectively independent of the Xe-vacancy cluster size. Due to the insensitivity of the diffusion coefficient on the cluster size, the diffusion coefficient of Xe in a vacancy cluster was obtained by averaging over all cluster sizes at each temperature. The calculated diffusion coefficients were also extrapolated to lower temperatures by fitting to an Arrhenius equation as shown in Fig. 4(a) and Table 1. The Xe-vacancy clusters evaluated in this

work were not large enough to be immobile. However, since it is known that a large enough Xe-vacancy cluster/bubble is immobile [66, 67], the largest cluster described in this work (Xe-tetradecavacancy) was treated as immobile in the radiation-enhanced diffusion calculations to approximate Xe segregation into large bubbles. For example, a 2 nm Xe bubble was found to be immobile in UO₂ [66]. Xe clusters containing more than 14 vacancies were not investigated to identify an immobile Xe-vacancy cluster due to the computational expense associated with conducting MD simulations of complex defects for 500 ns.

The statistical significance of the diffusion was verified in that linear dependencies of the mean-squared displacement as a function of time were achieved for all clusters, and visual inspection via OVITO [68] was performed to validate the observed results for the mean-squared displacements. Each individual Xe cluster displayed an Arrhenius relationship, albeit with a different pre-factor and migration energy. It is possible that rapid surface diffusion plays a role in the relative mobility of Xe-clusters with a large ($n > 4$) number of vacancies. It should also be noted that only Xe-clusters with a single Xe atom are investigated, and the diffusional behaviors of m Xe- n vacancy ($m > 1$) clusters could be quite different than Xe-vacancy clusters with a single Xe atom. It is presumed that such multi-Xe clusters would diffuse slower than the clusters investigated in this work, and as such the diffusion coefficients within the current study can be considered as an upper bound on the diffusion of possible Xe-vacancy clusters that can form under irradiation.

The averaged cluster diffusion coefficients from Fig. 9(a) and the cluster concentrations from Fig. 8 can now be used to calculate the radiation-enhanced diffusion coefficients of Xe in γ U-10Mo. These radiation-enhanced diffusivities are represented with respect to inverse temperature at three fission rate densities in Fig. 9(b). The radiation-enhanced diffusion of Xe is observed to be nearly athermal at high temperatures. Specifically, the athermal regime exists at temperatures greater than or equal to 600 K at 5×10^{18} fiss/m³/s, 700 K at 5×10^{20} fiss/m³/s, and 800 K at 5×10^{22} fiss/m³/s. This is attributed to the decreasing concentration of the smallest Xe-vacancy clusters (Xe-monovacancy), which dominated in this regime, while the diffusion coefficient of Xe in a vacancy cluster increased as the temperature increased. These offsetting contributions resulted in a near-constant radiation-enhanced diffusion of Xe. In the intermediate temperature regime, the radiation-enhanced diffusion of Xe increased with increasing temperature. This was due to the increase of the diffusion coefficient of Xe in a vacancy cluster, while the concentration of the biggest Xe-vacancy clusters (Xe-quadvacancy), which dominated in this regime, remained nearly constant. This tendency occurred within the temperature range between 350 K and 600 K at 5×10^{18} fiss/m³/s, 375 K and 700 K at 5×10^{20} fiss/m³/s, and 400 K and 800 K at 5×10^{22} fiss/m³/s. In the low-temperature regime, when compared to the intermediate temperature regime, the

radiation-enhanced diffusion of Xe increased more rapidly with increasing temperature since both the diffusion coefficient of Xe and the concentration of the smallest Xe-vacancy clusters (Xe-monovacancy), which dominated in this regime, increased. This behavior applied to temperatures less than or equal to 350 K at 5×10^{18} fiss/m³/s, 375 K at 5×10^{20} fiss/m³/s, and 400 K at 5×10^{22} fiss/m³/s.

516

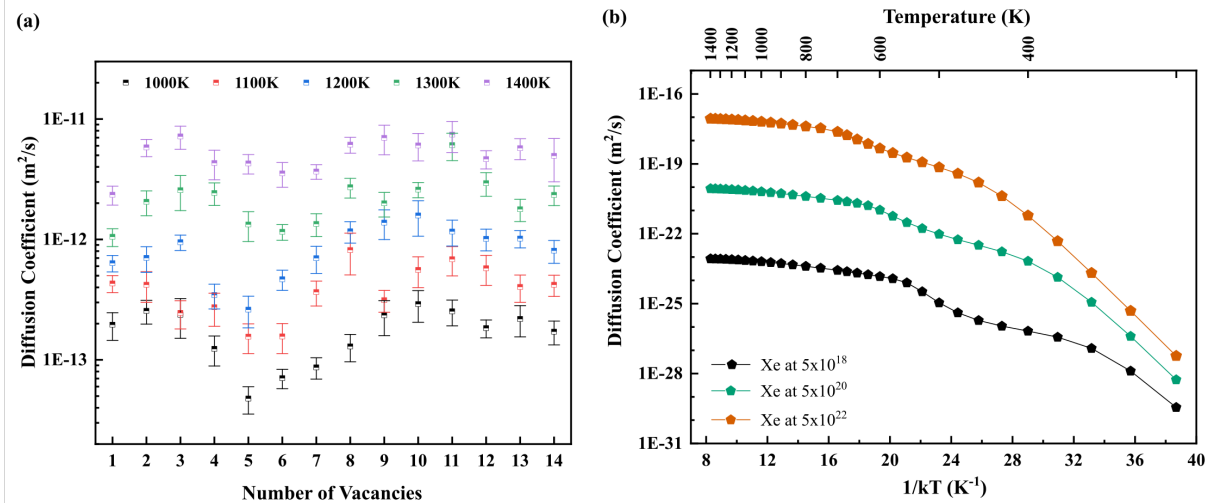


Figure 9: (a) Diffusion coefficient of a Xe-vacancy cluster with respect to size. (b) Radiation-enhanced diffusion of Xe in γ U-10Mo as a function of fission rate density (units are fiss/m³/s).

The radiation-enhanced diffusion of Xe is plotted along with the intrinsic thermal diffusion and radiation-driven diffusion of Xe in Fig. 10 (a)-(c), and the total diffusion coefficient of Xe under irradiation is represented in Fig. 10(d), all as a function of inverse temperature at three fission rate densities. It should be noted that the intrinsic Xe diffusion coefficients, both the previously assumed [28, 29] and calculated in this work, are represented in Fig. 10. The influence of the radiation-enhanced diffusion of Xe on the total diffusion was dependent on the fission rate density and the intrinsic thermal diffusion of Xe. The intrinsic thermal diffusion of Xe, calculated in this work, had a higher activation energy and was two to ten orders of magnitude slower than the previously assumed intrinsic thermal diffusion of Xe depending on the temperature (Fig. 10) [28, 29]. The results of the Arrhenius fits of the intrinsic thermal diffusion of Xe are compared in Table 2.

Utilizing the intrinsic thermal diffusion of Xe calculated in this work, the radiation-enhanced diffusion of Xe at 5×10^{18} fiss/m³/s (Fig. 10(a)) did not significantly contribute to the total diffusion of Xe at the investigated temperatures. For instance, the radiation-enhanced diffusion of Xe was approximately 30-100 times slower than the radiation-driven diffusion of Xe above 700 K. The intrinsic thermal diffusion of Xe began to dominate the diffusion processes above 950 K, whereas the radiation-driven diffusion of Xe began to dom-

inate below 950 K. For the fission rate density of 5×10^{20} fiss/m³/s (Fig. 10(b)), the intrinsic thermal diffusion of Xe dominated above 1150 K and the radiation-driven diffusion of Xe dominated below 1150 K. However, the contribution of the radiation-enhanced diffusion of Xe to the total diffusion increased as the fission rate density increased to 5×10^{20} fiss/m³/s (Fig. 10(b)). Specifically, the radiation-enhanced diffusion of Xe was slower than the radiation-driven diffusion of Xe by only a factor of 3-10 above 700 K. As the fission rate density increased further to 5×10^{22} fiss/m³/s (Fig. 10(c)), the radiation-enhanced diffusion of Xe exceeded both the intrinsic thermal diffusion and the radiation-driven diffusion of Xe at temperatures above 700 K.

The radiation-enhanced diffusion and the radiation-driven diffusion of Xe were also compared to the previously utilized intrinsic thermal diffusion of Xe [28, 29]. Since this estimate for intrinsic diffusion is significantly faster than the values calculated in this work, the temperature range where intrinsic diffusion becomes dominant occurs at a consistently lower temperature for all fission rate densities. Radiation-enhanced diffusion was not a dominant mode of diffusion for any temperatures for the fission rates of 5×10^{18} and 5×10^{20} fiss/m³/s. As the fission rate density increased further to 5×10^{22} fiss/m³/s (Fig. 10(c)), the radiation-enhanced diffusion of Xe exceeded the intrinsic thermal diffusion and the radiation-driven diffusion of Xe in the temperature range between 700 K to 1100 K. Thus, the previously utilized Xe diffusion assumptions underestimate the potential importance of radiation-enhanced diffusion.

The differences in the radiation-affected diffusion of U and Mo as compared to Xe are quite stark, especially when considering the respective trends as a function of the fission rate. As mentioned previously, in both U and Mo, a square-root and linear relationship were observed in the radiation-enhanced diffusion and radiation-driven diffusion with respect to fission rate density, respectively. However, in the case of Xe, it becomes more complicated due to the interaction of vacancies with Xe and Xe-vacancy clusters, which created non-uniform variability as a function of fission rate density and temperature.

561

Table 2: Arrhenius fit of intrinsic thermal diffusion of Xe in γ U-10Mo.

	Activation energy (eV)	Pre-exponential factor (m ² /s)
Previous assumption [28, 29]	1.76	1.28×10^{-9}
This work	2.30	6.53×10^{-10}

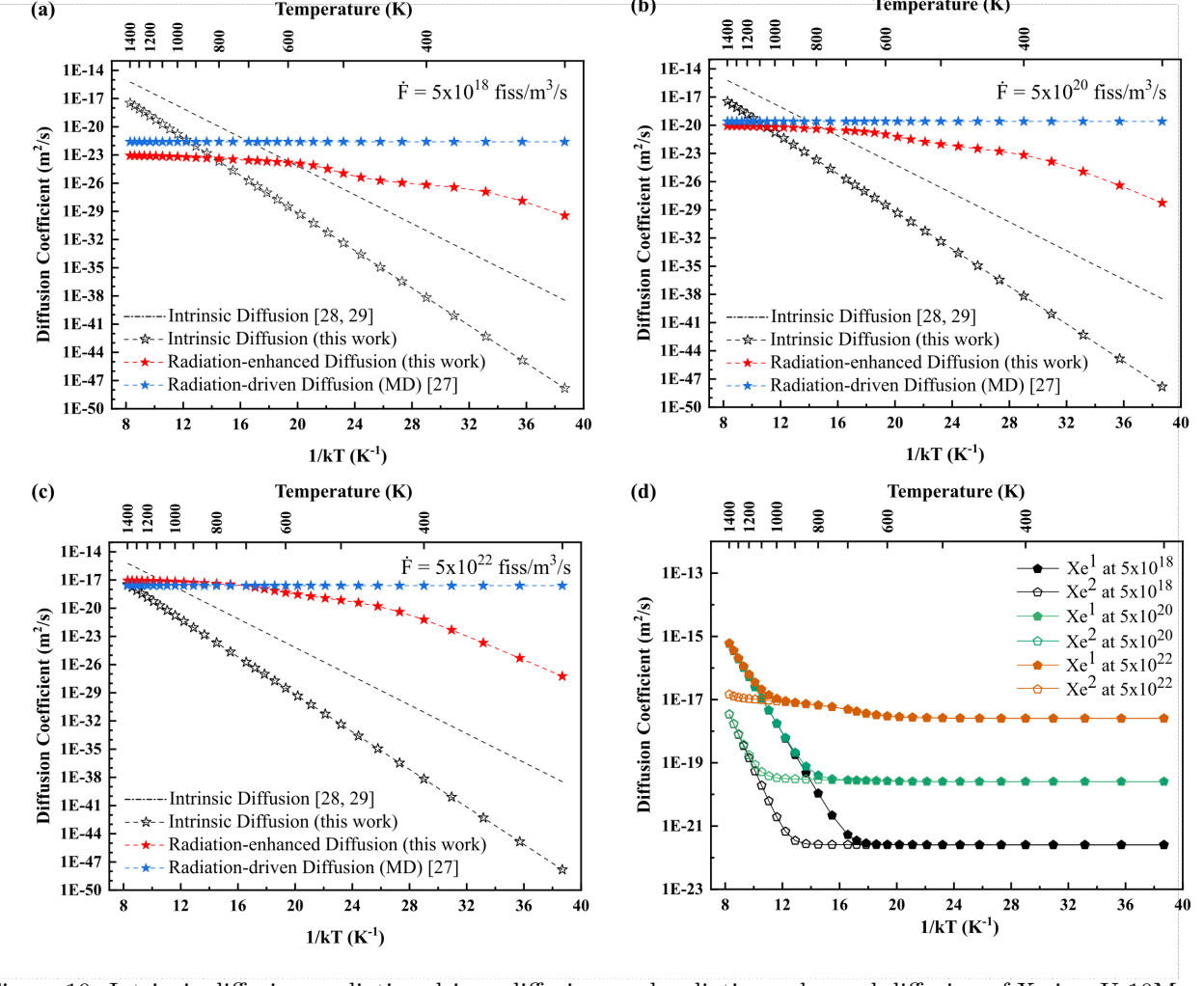


Figure 10: Intrinsic diffusion, radiation-driven diffusion, and radiation-enhanced diffusion of Xe in γ U-10Mo at (a) $5 \times 10^{18} \text{ fiss}/\text{m}^3/\text{s}$, (b) $5 \times 10^{20} \text{ fiss}/\text{m}^3/\text{s}$, and (c) $5 \times 10^{22} \text{ fiss}/\text{m}^3/\text{s}$. (d) Total diffusion of Xe as a function of fission rate density ($\text{fiss}/\text{m}^3/\text{s}$). Note the differences in the y scales. Xe^1 is calculated from the previous assumption, and Xe^2 is calculated in this work [28, 29].

562 4. Discussion

563 Radiation-enhanced diffusion of Xe behaved differently as compared to radiation-enhanced
 564 diffusion of U and Mo with respect to temperature and fission rate density in γ U-10Mo. The
 565 intrinsic thermal diffusion, radiation-enhanced diffusion, and radiation-driven diffusion of U
 566 and Mo dominated in the high, intermediate, and low-temperature regimes, respectively,
 567 depending on the fission rate density as described in Section 3.2. Given that the reactor
 568 operating temperature is below approximately 150°C and the fission rate density is on the
 569 order of $10^{20} \text{ fiss}/\text{m}^3/\text{s}$ in research reactors, both radiation-enhanced diffusion and radiation-
 570 driven diffusion of U and Mo contribute to species mobility under irradiation at all relevant
 571 research reactor temperatures and fission rate densities [3, 69]. On the other hand, the
 572 radiation-enhanced diffusion of Xe did not significantly impact the diffusion under irradiation.

ation at relevant temperatures and fission rate densities in research reactors. Alternately, radiation-driven diffusion of Xe dominated the diffusion process of Xe for relevant operating conditions in research reactors. For the establishment of future models, the intrinsic thermal diffusion of each element can likely be neglected in research reactors due to the specific operating parameters (temperature and fission rate density) which dictate the prevalence of irradiation-assisted diffusion.

Radiation-enhanced diffusion was previously investigated in other fuel materials such as UO_2 [26, 33] and U_3Si_2 [34]. In UO_2 , it was observed that radiation-enhanced diffusion of Xe dominated over the intrinsic thermal diffusion of Xe below 1561 K at the fission rate density of 10^{19} fiss/m³/s from experiments [24], which is inconsistent with the Xe observations in this work. Anderson et al. [33] predicted the radiation-enhanced diffusion of Xe via cluster dynamics parametrized by DFT and MD simulations, which agreed well with experimental observations. For example, the radiation-enhanced diffusion of Xe dominated over the intrinsic diffusion of Xe below 1771 K at the identical fission rate density in UO_2 [24, 33]. In addition, the radiation-enhanced diffusion of U in UO_2 dominated between 1250 K and 1800 K at 10^{19} fiss/m³/s [34]. This work established credibility for the prediction of Xe radiation-enhanced diffusion via strictly computational pathways. In the U_3Si_2 system, radiation-enhanced diffusion of U and Si did not significantly contribute to the total diffusion at the evaluated fission rate densities from 10^{17} fiss/m³/s to 10^{19} fiss/m³/s [26], which is in qualitative agreement with the behavior of Xe in this work. The radiation-driven diffusion of U and Si was greater than the radiation-enhanced diffusion of U and Si by 4-5 orders of magnitude [26]. Uranium diffusion was faster than Si diffusion, and diffusion occurred primarily via interstitials rather than vacancies in U_3Si_2 [26, 43]. The relative similarities of U-10Mo to the U_3Si_2 system, specifically both having metallic bonding and interstitial-based self-diffusion, suggest that the irradiation-affected diffusion behaviors would also show some similarities, which is confirmed in this work.

A comment should be made to contextualize some of the assumptions made, and some of the results observed, in this work. To calculate the radiation-enhanced diffusion of Xe, rate-theory equations (Eqs. 13-19) were constructed to calculate the steady-state concentrations of defects, comprising vacancies, interstitials, Xe, and Xe-vacancy clusters in the fuel under irradiation. However, unlike the concentrations of vacancies and interstitials, the concentrations of Xe-vacancy clusters did not reach a steady-state value since Xe was continuously produced, and only small Xe-vacancy clusters were considered in the rate-theory equations. Experimentally, it is expected that the concentration of Xe will increase with respect to time under irradiation since Xe is continually produced via fission, but fission gas release does not occur in the U-Mo fuel system. Thus, the concentrations at the time of

609 45 days, which is approximately the time at which U-10Mo fuel undergoes recrystallization
610 in research reactors, are utilized in the determination of radiation enhanced diffusion of Xe
611 [16, 70, 71, 72, 73]. In addition, the presence of large fission gas bubbles is not explicitly
612 taken into account in the rate-theory equations. Point defects (vacancies and interstitials)
613 and Xe will diffuse into fission gas bubbles, as well as grain boundaries, which are the pri-
614 mary sinks in the fuel, and losses of point defects and Xe will likely decrease the Xe-vacancy
615 cluster concentrations under irradiation. Thus, this work represents an upper bound of the
616 possible radiation-enhanced diffusion of Xe, with a series of assumptions that likely exagge-
617 rate the rate at which Xe and Xe-vacancy clusters are able to be transported in U-Mo fuel.
618 This, combined with the limited range of prevalence of radiation-enhanced diffusion for Xe
619 in U-Mo, indicates that it is highly likely that the radiation-driven diffusion of Xe will be
620 the dominant mode of Xe diffusion at temperatures relevant to research reactors.

621

622 5. Summary and Conclusions

623 In the present work, the radiation-enhanced diffusion coefficients of U, Mo, and Xe in
624 γ U-10Mo were calculated using rate-theory models and MD simulations with the ternary U-
625 Mo-Xe interatomic potential [38] in the temperature range between 300 K and 1400 K and
626 the fission rate density range between 5×10^{18} fiss/m³/s and 5×10^{22} fiss/m³/s. The calculated
627 radiation-enhanced diffusion coefficient of each element was compared to the intrinsic thermal
628 diffusion and the radiation-driven diffusion, determined previously [27, 30]. The intrinsic
629 thermal diffusion of Xe was calculated using the concentration of vacancies at equilibrium
630 and the diffusion coefficient of Xe in a monovacancy cluster. The total diffusion of U, Mo, and
631 Xe under irradiation conditions were also determined by summing the radiation-enhanced
632 diffusion, calculated in this work, and the previously determined intrinsic thermal diffusion
633 and radiation-driven diffusion [27, 30]. It was found that both radiation-enhanced diffusion
634 and radiation-driven diffusion of U and Mo dominated at the operating temperatures and
635 typical fission rate densities of research reactors. The influence of the radiation-enhanced
636 diffusion of Xe on the total diffusion of Xe under irradiation increased with increasing fission
637 rate density. However, the radiation-enhanced diffusion of Xe did not significantly contribute
638 to the total diffusion of Xe at a fission rate density of 5×10^{18} fiss/m³/s and 5×10^{20} fiss/m³/s.
639 The radiation-enhanced diffusion of Xe exceeded the intrinsic diffusion of Xe, calculated in
640 this work, as well as the radiation-driven diffusion of Xe at 5×10^{22} fiss/m³/s above 700 K,
641 although, this is likely beyond the fission rate density regime that is obtained within research
642 reactors. The total diffusion coefficients of U, Mo, and Xe in γ U-10Mo, updated in this work,
643 will be utilized as important parameters in mechanistic fuel models, as well as potentially

644 in other nuclear fuel mesoscale models, such as kinetic Monte Carlo, phase-field models,
645 cluster dynamics, and finite element analysis, to predict the microstructural evolution under
646 irradiation more accurately.

647 **6. CRediT author statement**

648 **Gyuchul Park:** Conceptualization, Formal analysis, Software, Investigation, Methodology,
649 Visualization, Writing-original draft. **Benjamin Beeler:** Conceptualization, Funding
650 acquisition, Methodology, Project administration, Resources, Supervision, Writing-review
651 and editing. **Maria A. Okuniewski:** Conceptualization, Funding acquisition, Methodology,
652 Project administration, Resources, Supervision, Writing-review and editing.

653 **7. Acknowledgements**

654 This work was supported by the U.S. Department of Energy, Office of Material Management
655 and Minimization, National Nuclear Security Administration, under DOE-NE Idaho
656 Operations Office Contract DE-AC07-05ID14517. This research made use of the High-
657 Performance Computing Center at Idaho National Laboratory, which is supported by the
658 Office of Nuclear Energy of the U.S. Department of Energy and the Nuclear Science User
659 Facilities.

660 Appendix A.

661 The concentration of vacancies, interstitials, and Xe clusters as a function of inverse
 662 temperature at three fission rate densities is shown in Fig. A.1, including data for all Xe-
 663 vacancy clusters investigated.

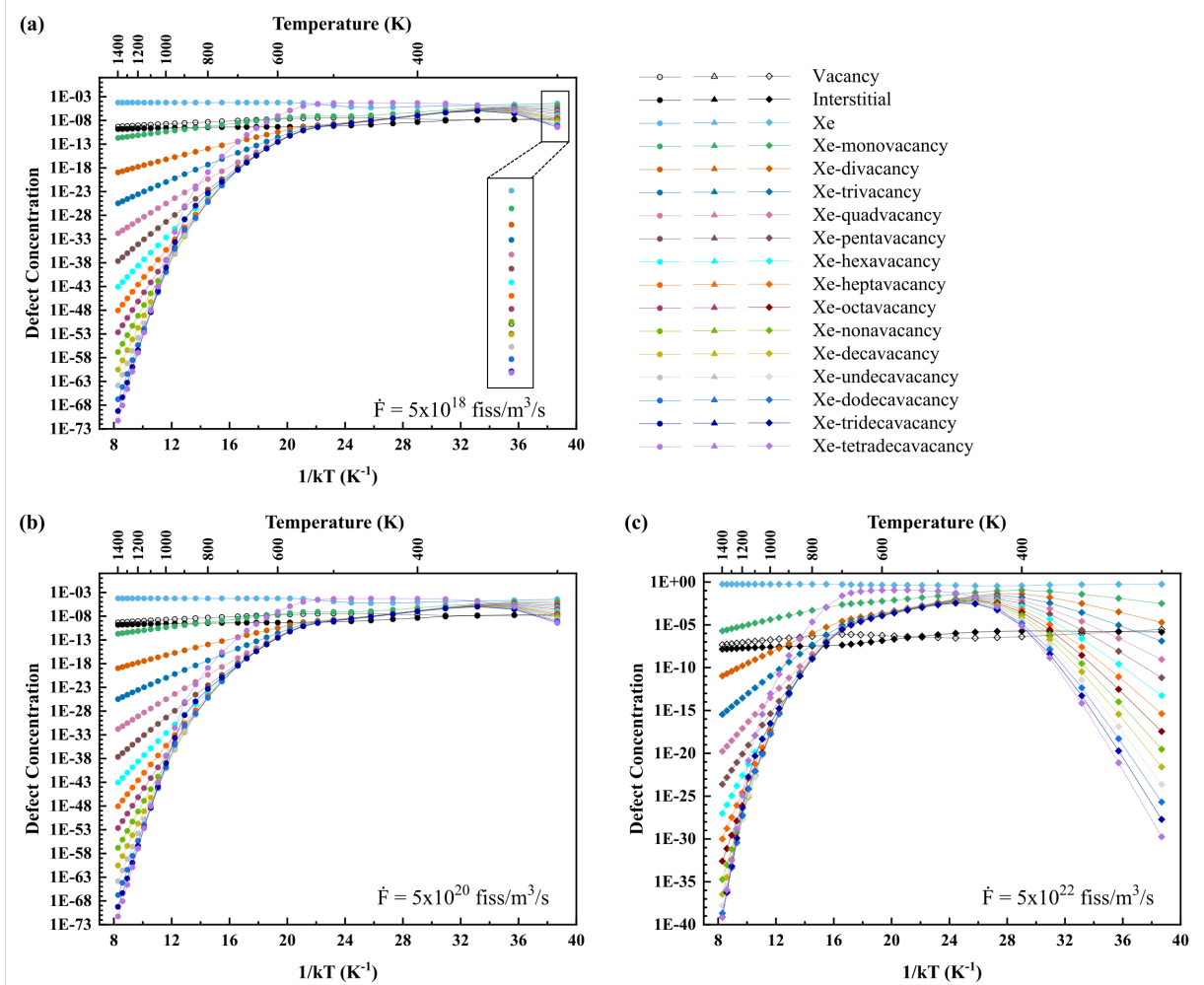


Figure A.1: Evolution of concentrations of vacancies, interstitials, Xe, and Xe-vacancy clusters in γ U-10Mo as a function of inverse temperature at (a) 5×10^{18} fiss/m³/s, (b) 5×10^{20} fiss/m³/s, and (c) 5×10^{22} fiss/m³/s. The Xe-vacancy clusters containing up to 14 vacancies (Xe-tetradecavacancy) are considered.

664 **References**

- 665 [1] Y. S. Kim, G. L. Hofman, Fission product induced swelling of U–Mo alloy fuel, Journal
666 of Nuclear Materials 419 (1–3) (2011) 291–301.
- 667 [2] A. Robinson, D. Perez, D. Porter, et al., Irradiation Performance of U–Mo Alloy Based
668 ‘Monolithic’ Plate-Type-Design Selection Update, Tech. Rep. No. INL/EXT-09-16807,
669 Idaho National Lab.(INL), Idaho Falls, ID (United States) (2013).
- 670 [3] M. Meyer, J. Gan, J. Jue, D. Keiser, E. Perez, A. Robinson, D. Wachs, N. Woolsten-
671 hulme, G. Hofman, Y. Kim, Irradiation performance of U–Mo monolithic fuel, Nuclear
672 Engineering and Technology 46 (2) (2014) 169–182.
- 673 [4] D. Keiser, J.-F. Jue, B. Miller, J. Gan, A. Robinson, J. Madden, Observed changes in
674 as-fabricated U–10Mo monolithic fuel microstructures after irradiation in the advanced
675 test reactor, JOM 69 (12) (2017) 2538–2545.
- 676 [5] R. Prabhakaran, U–Mo monolithic fuel for nuclear research and test reactors, JOM
677 69 (12) (2017) 2529–2531.
- 678 [6] J.-F. Jue, D. D. Keiser Jr, B. D. Miller, J. W. Madden, A. B. Robinson, B. H. Rabin,
679 Effects of irradiation on the interface between U–Mo and zirconium diffusion barrier,
680 Journal of Nuclear Materials 499 (2018) 567–581.
- 681 [7] C. Miller, B. Durtschi, J. I. Cole, K. Daum, U–10Mo Monolithic Fuel Qualification Plan,
682 Tech. Rep. No. INL/EXT-13-30238-Rev003, Idaho National Lab.(INL), Idaho Falls, ID
683 (United States) (2021).
- 684 [8] J. Gan, B. Miller, D. Keiser Jr, J. Jue, J. Madden, A. Robinson, H. Ozaltun, G. Moore,
685 M. Meyer, Irradiated microstructure of U–10Mo monolithic fuel plate at very high fission
686 density, Journal of Nuclear Materials 492 (2017) 195–203.
- 687 [9] J. J. Giglio, USHPRR MP-1: Observations from PIE and path forward for the MP-2
688 Experiment and Experimental Summary, Tech. Rep. No. INL/EXT-21-61324-Rev000,
689 Idaho National Lab.(INL), Idaho Falls, ID (United States) (2021).
- 690 [10] K. Nordlund, S. J. Zinkle, A. E. Sand, F. Granberg, R. S. Averback, R. E. Stoller,
691 T. Suzudo, L. Malerba, F. Banhart, W. J. Weber, F. Willaime, S. L. Dudarev, D. Sime-
692 one, Primary radiation damage: A review of current understanding and models, Journal
693 of Nuclear Materials 512 (2018) 450–479.

- 694 [11] Y. Kim, G. Hofman, J. Rest, G. Shevlyakov, S. RIAR, et al., Characterization of in-
695 tergranular fission gas bubbles in U-Mo fuel., Tech. Rep. No. ANL-08/11, Argonne
696 National Lab.(ANL), Argonne, IL (United States) (2008).
- 697 [12] S. Van den Berghe, W. Van Renterghem, A. Leenaers, Transmission electron microscopy
698 investigation of irradiated U-7 wt% Mo dispersion fuel, Journal of Nuclear Materials
699 375 (3) (2008) 340–346.
- 700 [13] J. Gan, D. D. Keiser Jr, D. M. Wachs, A. B. Robinson, B. D. Miller, T. R. Allen,
701 Transmission electron microscopy characterization of irradiated U-7Mo/Al-2Si disper-
702 sion fuel, Journal of Nuclear Materials 396 (2-3) (2010) 234–239.
- 703 [14] D. Olander, D. Wongsawaeng, Re-solution of fission gas—A review: Part I. Intragranular
704 bubbles, Journal of Nuclear Materials 354 (1-3) (2006) 94–109.
- 705 [15] J. Rest, A model for the effect of the progression of irradiation-induced recrystallization
706 from initiation to completion on swelling of UO_2 and U-10Mo nuclear fuels, Journal of
707 Nuclear Materials 346 (2-3) (2005) 226–232.
- 708 [16] Y. S. Kim, G. Hofman, J. Cheon, Recrystallization and fission-gas-bubble swelling of
709 U-Mo fuel, Journal of Nuclear Materials 436 (1-3) (2013) 14–22.
- 710 [17] L. Liang, Z.-G. Mei, Y. S. Kim, B. Ye, G. Hofman, M. Anitescu, A. M. Yacout, Mesoscale
711 model for fission-induced recrystallization in U-7Mo alloy, Computational Materials
712 Science 124 (2016) 228–237.
- 713 [18] S. Hu, C. H. Henager Jr, H. L. Heinisch, M. Stan, M. I. Baskes, S. M. Valone, Phase-field
714 modeling of gas bubbles and thermal conductivity evolution in nuclear fuels, Journal of
715 Nuclear Materials 392 (2) (2009) 292–300.
- 716 [19] S. Hu, D. E. Burkes, C. A. Lavender, D. J. Senor, W. Setyawan, Z. Xu, Formation mech-
717 anism of gas bubble superlattice in UMo metal fuels: Phase-field modeling investigation,
718 Journal of Nuclear Materials 479 (2016) 202–215.
- 719 [20] L. Liang, Z.-G. Mei, Y. S. Kim, M. Anitescu, A. M. Yacout, Three-dimensional phase-
720 field simulations of intragranular gas bubble evolution in irradiated U-Mo fuel, Compu-
721 tational Materials Science 145 (2018) 86–95.
- 722 [21] L. Liang, Y. S. Kim, Z.-G. Mei, L. K. Aagesen, A. M. Yacout, Fission gas bubbles and
723 recrystallization-induced degradation of the effective thermal conductivity in U-7Mo
724 fuels, Journal of Nuclear Materials 511 (2018) 438–445.

- 725 [22] B. Ye, J. Rest, Y. S. Kim, G. Hofman, B. Dionne, DART analysis of irradiation behavior
726 of U-Mo/Al dispersion fuels, Nuclear Technology 191 (1) (2015) 27–40.
- 727 [23] B. Ye, G. Hofman, A. Leenaers, A. Bergeron, V. Kuzminov, S. Van den Berghe, Y. Kim,
728 H. Wallin, A modelling study of the inter-diffusion layer formation in U-Mo/Al disper-
729 sion fuel plates at high power, Journal of Nuclear Materials 499 (2018) 191–203.
- 730 [24] J. Turnbull, C. Friskney, J. Findlay, F. Johnson, A. Walter, The diffusion coefficients
731 of gaseous and volatile species during the irradiation of uranium dioxide, Journal of
732 Nuclear Materials 107 (2-3) (1982) 168–184.
- 733 [25] R. Perriot, C. Matthews, M. W. Cooper, B. P. Uberuaga, C. R. Stanek, D. A. Andersson,
734 Atomistic modeling of out-of-pile xenon diffusion by vacancy clusters in UO_2 , Journal
735 of Nuclear Materials 520 (2019) 96–109.
- 736 [26] M. W. D. Cooper, K. A. Gamble, L. Capolungo, C. Matthews, D. Andersson, B. Beeler,
737 C. R. Stanek, K. Metzger, Irradiation-enhanced diffusion and diffusion-limited creep in
738 U_3Si_2 , Journal of Nuclear Materials 555 (2021) 153129.
- 739 [27] B. Beeler, M. W. Cooper, Z.-G. Mei, D. Schwen, Y. Zhang, Radiation driven diffusion
740 in $\gamma\text{U-Mo}$, Journal of Nuclear Materials 543 (2021) 152568.
- 741 [28] S. Hu, V. Joshi, C. Lavender, N. Lombardo, J. Wight, B. Ye, et al., Microstructural level
742 fuel performance modeling of UMo monolithic fuel, Tech. Rep. No. INL/LTD-16-40028,
743 Idaho National Lab.(INL), Idaho Falls, ID (United States) (2016).
- 744 [29] B. Beeler, J. Burks, J. Cole, Y. Gao, G. Hofman, V. Hu, Joshi, C. Lavendar, L. Liang,
745 N. Lombardo, Z.-G. Mei, A. Oaks, J. Wight, A. Yacout, B. Ye, Y. Zhang, Microstruc-
746 tural level fuel performance modeling of UMo monolithic fuel, Tech. Rep. No. INL/LTD-
747 18-51573, Idaho National Lab.(INL), Idaho Falls, ID (United States) (2018).
- 748 [30] K. Huang, J. D. Keiser, Y. Sohn, Interdiffusion, intrinsic diffusion, atomic mobility, and
749 vacancy wind effect in γ (bcc) uranium-molybdenum alloy, Metallurgical and Materials
750 Transactions A 44A (2013) 738.
- 751 [31] L. Kolotova, S. Starikov, Atomistic simulation of defect formation and structure trans-
752 sitions in U-Mo alloys in swift heavy ion irradiation, Journal of Nuclear Materials 495
753 (2017) 111–117.
- 754 [32] L. Kolotova, S. Starikov, V. Ozrin, Atomistic simulation of the fission-fragment-induced
755 formation of defects in a uranium–molybdenum alloy, Journal of Experimental and
756 Theoretical Physics 129 (1) (2019) 59–65.

- 757 [33] D. Andersson, P. Garcia, X.-Y. Liu, G. Pastore, M. Tonks, P. Millett, B. Dorado, D. Gaston, D. Andrs, R. Williamson, et al., Atomistic modeling of intrinsic and radiation-enhanced fission gas (Xe) diffusion in $UO_{2\pm x}$: Implications for nuclear fuel performance modeling, *Journal of Nuclear Materials* 451 (1-3) (2014) 225–242.
- 761 [34] C. Matthews, R. Perriot, W. Cooper, C. R. Stanek, D. A. Andersson, Cluster dynamics simulation of xenon diffusion during irradiation in UO_2 , *Journal of Nuclear Materials* 540 (2020) 152326.
- 764 [35] S. Plimpton, Fast parallel algorithms for short-range molecular dynamics, *Journal of Computational Physics* 117 (1) (1995) 1–19.
- 766 [36] M. S. Daw, M. I. Baskes, Semiempirical, quantum mechanical calculation of hydrogen embrittlement in metals, *Physical Review Letters* 50 (17) (1983) 1285.
- 768 [37] M. S. Daw, M. I. Baskes, Embedded-atom method: Derivation and application to impurities, surfaces, and other defects in metals, *Physical Review B* 29 (12) (1984) 6443.
- 770 [38] D. Smirnova, A. Y. Kuksin, S. Starikov, V. Stegailov, Z. Insepov, J. Rest, A. Yacout, A ternary EAM interatomic potential for U–Mo alloys with xenon, *Modelling and Simulation in Materials Science and Engineering* 21 (3) (2013) 035011.
- 773 [39] F. Ercolessi, J. B. Adams, Interatomic potentials from first-principles calculations: the force-matching method, *EPL (Europhysics Letters)* 26 (8) (1994) 583.
- 775 [40] N. Grønbech-Jensen, O. Farago, A simple and effective Verlet-type algorithm for simulating Langevin dynamics, *Molecular Physics* 111 (8) (2013) 983–991.
- 777 [41] N. Grønbech-Jensen, N. R. Hayre, O. Farago, Application of the G-JF discrete-time thermostat for fast and accurate molecular simulations, *Computer Physics Communications* 185 (2) (2014) 524–527.
- 780 [42] G. Park, B. Beeler, M. A. Okuniewski, An atomistic study of defect energetics and diffusion with respect to composition and temperature in γ U and γ U–Mo alloys, *Journal of Nuclear Materials* 552 (2021) 152970.
- 783 [43] D. Andersson, X.-Y. Liu, B. Beeler, S. Middleburgh, A. Claisse, C. R. Stanek, Density functional theory calculations of self-and Xe diffusion in U_3Si_2 , *Journal of Nuclear Materials* 515 (2019) 312–325.
- 786 [44] D. Andersson, B. Uberuaga, P. Nerikar, C. Unal, C. Stanek, U and Xe transport in $UO_{2\pm x}$: Density functional theory calculations, *Physical Review B* 84 (5) (2011) 054105.

- 788 [45] A. E. Thompson, C. Wolverton, Pathway and energetics of xenon migration in uranium
789 dioxide, *Physical Review B* 87 (10) (2013) 104105.
- 790 [46] R. Bès, P. Martin, E. Vathonne, R. Delorme, C. Sabathier, M. Freyss, M. Bertolus,
791 P. Glatzel, Experimental evidence of Xe incorporation in schottky defects in UO_2 , *Applied Physics Letters* 106 (11) (2015) 114102.
- 792
- 793 [47] B. Beeler, B. Good, C. Deo, S. Rashkeev, M. Baskes, M. Okuniewski, Formation and
794 incorporation energies of fission gases He, Xe, and Kr in bcc uranium, *Minerals, Metals
795 and Materials Society/AIME* (2011).
- 796 [48] B. Beeler, B. Good, S. Rashkeev, C. Deo, M. Baskes, M. Okuniewski, First-principles
797 calculations of the stability and incorporation of helium, xenon and krypton in uranium,
798 *Journal of Nuclear Materials* 425 (1-3) (2012) 2–7.
- 799 [49] B. Beeler, S. Hu, Y. Zhang, Y. Gao, A improved equation of state for Xe gas bubbles
800 in γU -Mo fuels, *Journal of Nuclear Materials* 530 (2020) 151961.
- 801 [50] G. Wanner, E. Hairer, *Solving ordinary differential equations II*, Vol. 375, Springer
802 Berlin Heidelberg New York, 1996.
- 803 [51] J. Bezanson, A. Edelman, S. Karpinski, V. B. Shah, Julia: A fresh approach to numerical
804 computing, *SIAM review* 59 (1) (2017) 65–98.
- 805 [52] K. Nordlund, S. J. Zinkle, A. E. Sand, F. Granberg, R. S. Averback, R. Stoller,
806 T. Suzudo, L. Malerba, F. Banhart, W. J. Weber, F. Willaime, S. L. Dudarev, D. Sime-
807 one, Improving atomic displacement and replacement calculations with physically real-
808 istic damage models, *Nature Communications* 9 (1) (2018) 1–8.
- 809 [53] M. Norgett, M. Robinson, I. Torrens, A proposed method of calculating displacement
810 dose rates, *Nuclear Engineering and Design* 33 (1) (1975) 50–54.
- 811 [54] B. Beeler, Y. Zhang, M. Okuniewski, C. Deo, Calculation of the displacement energy of
812 α and γ uranium, *Journal of Nuclear Materials* 508 (2018) 181–194.
- 813 [55] Y. Zhang, H. Huang, P. C. Millett, M. Tonks, D. Wolf, S. R. Phillpot, Atomistic study
814 of grain boundary sink strength under prolonged electron irradiation, *Journal of Nuclear
815 Materials* 422 (1-3) (2012) 69–76.
- 816 [56] H. Kleykamp, The chemical state of the fission products in oxide fuels, *Journal of
817 Nuclear Materials* 131 (2-3) (1985) 221–246.

- 818 [57] A. Nichols, M. Verpelli, D. Aldama, Handbook of nuclear data for safeguards: database
819 extensions, August 2008, IAEA, 2008.
- 820 [58] B. Beeler, J. Cole, W. Frazier, Y. Gao, I. Glagolenko, G. Hofman, S. Hu, V. Joshi,
821 C. Lavendar, N. Lombardo, S. Masengale, Z. Mei, A. Oaks, M. Okuniewski, G. Park,
822 K. Verner, A. Yacout, B. Ye, Y. Zhang, Microstructural-level fuel performance modeling
823 of UMo monolithic fuel, Tech. Rep. No. INL/EXT-20-60591, Idaho National Lab.(INL),
824 Idaho Falls, ID (United States) (2020).
- 825 [59] X.-M. Bai, H. Ke, Y. Zhang, B. W. Spencer, Modeling copper precipitation hardening
826 and embrittlement in a dilute Fe-0.3 at.% Cu alloy under neutron irradiation, Journal
827 of Nuclear Materials 495 (2017) 442–454.
- 828 [60] G. S. Was, Fundamentals of radiation materials science: metals and alloys, Springer,
829 2016.
- 830 [61] D. Smirnova, A. Y. Kuksin, S. Starikov, Investigation of point defects diffusion in bcc
831 uranium and U–Mo alloys, Journal of Nuclear Materials 458 (2015) 304–311.
- 832 [62] K. Yu, Y. Liu, C. Sun, H. Wang, L. Shao, E. Fu, X. Zhang, Radiation damage in
833 helium ion irradiated nanocrystalline Fe, Journal of Nuclear Materials 425 (1-3) (2012)
834 140–146.
- 835 [63] K. Nakashima, R. E. Stoller, H. Xu, Recombination radius of a frenkel pair and capture
836 radius of a self-interstitial atom by vacancy clusters in bcc Fe, Journal of Physics:
837 Condensed Matter 27 (33) (2015) 335401.
- 838 [64] M. Veshchunov, A. Boldyrev, A. Kuznetsov, V. Ozrin, M. Seryi, V. Shestak, V. Tarasov,
839 G. Norman, A. Y. Kuksin, V. Pisarev, et al., Development of the advanced mechanistic
840 fuel performance and safety code using the multi-scale approach, Nuclear Engineering
841 and Design 295 (2015) 116–126.
- 842 [65] D. Smirnova, A. Y. Kuksin, S. Starikov, V. Stegailov, Atomistic modeling of the self-
843 diffusion in γ -U and γ -U-Mo, The Physics of Metals and Metallography 116 (5) (2015)
844 445–455.
- 845 [66] C. Baker, The migration of intragranular fission gas bubbles in irradiated uranium
846 dioxide, Journal of Nuclear Materials 71 (1) (1977) 117–123.
- 847 [67] D.-U. Kim, S. Blondel, D. E. Bernholdt, P. Roth, F. Kong, D. Andersson, M. R. Tonks,
848 B. D. Wirth, Modeling mesoscale fission gas behavior in UO_2 by directly coupling the

- 849 phase field method to spatially resolved cluster dynamics, Materials Theory 6 (1) (2022)
850 1–28.
- 851 [68] A. Stukowski, Visualization and analysis of atomistic simulation data with OVITO—the
852 Open Visualization Tool, Modelling and Simulation in Materials Science and Engineering 18 (1) (2009) 015012.
- 853
- 854 [69] M. A. Marshall, M. A. Lillo, New As-run Neutronics Analysis for RERTR-12 Fuel Foil
855 Experiments, Tech. Rep. No. INL/CON-15-36359-Rev000, Idaho National Lab.(INL),
856 Idaho Falls, ID (United States) (2016).
- 857 [70] A. Leenaers, W. Van Renterghem, S. Van den Berghe, High burn-up structure of U(Mo)
858 dispersion fuel, Journal of Nuclear Materials 476 (2016) 218–230.
- 859 [71] D. Perez, M. Lillo, G. Chang, N. Woolstenhulme, RERTR-12 Insertion 1 Irradiation
860 Summary Report, Tech. Rep. No. INL/EXT-11-24101IN, Idaho National Lab.(INL),
861 Idaho Falls, ID (United States) (2012).
- 862 [72] D. Perez, G. Chang, D. Wachs, G. Roth, N. Woolstenhulme, RERTR-12 Insertion
863 2 Irradiation Summary Report, Tech. Rep. No. INL/EXT-12-27085, Idaho National
864 Lab.(INL), Idaho Falls, ID (United States) (2012).
- 865 [73] C. A. Smith, S. Biswas, B. D. Miller, B. Kombaiah, D. Frazer, D. D. Keiser,
866 A. Aitkaliyeva, High burnup structure formation in U-Mo fuels, Journal of Nuclear
867 Materials 563 (2022) 153617.